Performance, Modeling, and Characteristics of LFP pack for HEV using FUDS (depleting) in Hot and Arid Conditions

by

Andrew Opitz

A Thesis Presented in Partial Fulfillment
of the Requirements for the Degree
Master of Science

Approved June 2016 by the
Graduate Supervisory Committee:

Arunachala Kannan, Chair
Abdel Ra'ouf Mayyas
Changho Nam

ARIZONA STATE UNIVERISTY

August 2016

ABSTRACT

There was a growing trend in the automotive market on the adoption of Hybrid Electric Vehicles (HEVs) for consumers to purchase. This was partially due to external pressures such as the effects of global warming, cost of petroleum, governmental regulations, and popularity of the vehicle type. HEV technology relied on a variety of factors which included the powertrain (PT) of the system, external driving conditions, and the type of driving pattern being driven. The core foundation for HEVs depended heavily on the battery pack and chemistry being adopted for the vehicle performance and operations. This paper focused on the effects of hot and arid temperatures on the performance of $LiFePO_4$ (LFP) battery packs and presented a possible modeling method for overall performance.

Lithium-ion battery (LIB) packs were subjected to room and high temperature settings while being cycled under a current profile created from a drive cycle. The Federal Urban Driving Schedule (FUDS) was selected and modified to simulate normal city driving situation using an electric only drive mode. Capacity and impedance fade of the LIB packs were monitored over the lifetime of the pack to determine the overall performance through the variables of energy and power fade. Regression analysis was done on the energy and power fade of the LIB pack to determine the duration life of LIB packs for HEV applications. This was done by comparing energy and power fade with the average lifetime mileage of a vehicle.

The collected capacity and impedance data was used to create an electrical equivalent model (EEM). The model was produced through the process of a modified Randles circuit and the creation of the inverse constant phase element (ICPE). Results indicated the model had a potential for high fidelity as long as a sufficient amount of data was gathered. X-ray powder diffraction (XRD) and a scanning electron microscope (SEM) was performed on a fresh and cycled LFP battery. SEM results suggested a dramatic growth on LFP crystals with a reduction in carbon coating after cycling. XRD effects showed a slight uniformed strain and decrease in size of LFP olivine crystals after cycling.

ACKNOWLEDGMENTS

I would like to express a heart filled gratitude to Dr. Arunachalandar Madakannan, Dr. Abdel Ra'ouf Mayyas, and Dr. Changho Nam because I would not be where I am without them. My committee's unwavering support and guidance were paramount in the completion of writing my thesis. I was encouraged to seek excellence and to grasp for greatness. This allowed me to push the boundaries of known science and engineering a little bit further. I am truly thankful for the time I have had to learn from these great men and I wish them the best in life.

Secondly, I would like to thank the Salt River Project (SRP) for sponsoring my thesis project on hybrid electric vehicle and potential future energy storage. It was my hope that my research and results from the experiment were able to aid SRP with future endeavors as well as expanding the possibility of a more technologically advanced future.

Additional thanks should be given to Arizona State University for providing an innovative environment that allowed me to achieve greatness and to improve myself by seeking more knowledge.

I would like to send out my appreciation and thanks to my family, friends, students I worked with, my significant other, and God. My family cheered me on through the entire process including the good times and bad times which helped maintain the foundation I needed. I am thankful for my friends that listened to my difficulties, stayed up with me while I worked on my project, and playful jested with me about my situation. I want to

thank all of the graduate students that I worked with throughout my graduate career because they prepared me for situations later in life and challenged me to be my best. I would like to warmly thank my significant other for being my lighthouse on a dark and foggy night and a welcoming smile on a clear day. Lastly, I would like to express joy and thankfulness to God because through him, all things are possible.

TABLE OF CONTENTS

Page

APPENDIX Page

LIST OF TABLES

Table Page

LIST OF FIGURES

Figure Page

LIST OF SYMBOLS ABBREVIATIONS

Electric Vehicle: EV

Hybrid Electric Vehicle: HEV

Plug-in Hybrid Electric Vehicle: PHEV

Internal Combustion Engine: ICE

Electrochemical: EC

Automotive Batteries: AB

Automotive Application: AA

Electrical Energy: EE

Half-Cell: HC

Nominal Cell Voltage: NCV

Zinc-Carbon: ZC

Lead Acid: Pb acid

Nickel Cadmium: NiCd

Nickel Metal Hydride: NiMH

Lithium-ion: Li-ion

$LiFePO_4$: LFP

$LiCoO_2$: LCO

$LiMn_2O_4$: LMO

$LiNi_{0.8}Co_{0.15}Al_{0.05}O_2$: NCA

Urban Dynamometer Driving Schedule: UDDS

$LiNiCoMnO_2$: NCM

State of Health: SOH

Electrical Equivalent Model: EEM

Electrochemical Impedance Spectroscopy: EIS

Constant Phase Element: CPE

Federal Urban Driving Schedule: FUDS

Lithium-Ion Battery: LIB

Environmental Protection Agency: EPA

Federal Test Procedure: FTP

Highway Fuel Economy Test: HWFET

Highway Fuel Economy Driving Schedule: HFEDS

Supplemental Federal Test Procedure: SFTP

Inverse Constant Phase Element: ICPE

Butterworth-Van Dyke: BVD

X-Ray Powder Diffraction: XRD

Pure Electric Vehicles: PEV

Electric Motor: EM

Power-Train: PT

Scanning Electron Microscope: SEM

Full Width at Half Maximum: FWHM

1 INTRODUCTION

"The electric vehicle is not for everybody. It can only meet the needs of ninety percent of the population" – Ed Begley Jr. This quote was taken from the film called, "Who Killed the Electric Car?", which came out in late January 2006. Ed Begley Jr. expressed his sarcasm about the situation and how he believed that EVs should be invested into for the future of the automotive industry. Initially when EVs were first introduced to the market, they had a quarter of the sales because they were in a competition for control with steam and gasoline powered vehicles [1]. The reason why EVs were popular back then was consumer were concerned with the vehicles being comfortable while maintaining a short driving range throughout the few urban areas.

This made EVs superior compared to the competitors, but advancements in technology and improvements to infrastructure drove away EV acceptance. The development of the Ford Model T made cars affordable for the average person, a large supply of gasoline found in Texas dropped prices dramatically, and the construction of the modern highway provided farther places to travel. The modern day revival of EVs began around 1970s until the early 2000s where high cost of oil incentivized alternative vehicles until prices dropped again [1]. This was not the first attempt at popularizing EVs since their creation nearly 200 years ago, and it was not there last. Fast-forward to the year 2016, EVs were still on the market, sales were steadily growing, and were expecting to continue to grow.

There was an abundant amount of EVs offered in the vehicle market including micro, mild, plug-in, and pure electric. The size of the battery pack depends on the power

demand of the design which will be discussed in ascending order from smallest to largest. A micro hybrid features start-stop technology which starts the vehicle using the power from the battery packs [2]. This feature allowed the electrical systems to run if the ICE has stopped and the namesake for the technology. A tier higher than the micro hybrid was the mild hybrid which incorporates the same features, but had been designed for a series, or parallel drivetrain as well as regenerative braking [3].

Regenerative breaking allowed the HEV to charge the battery pack whenever enough braking forces had been applied during vehicle operation. The plug-in hybrid had equivalent characteristics as well as the option to charge from the grid and a charge depleting mode [4]. A charge depleting mode granted the EV to run on the battery pack only to sustain momentum. Two major drivetrain architectures for most HEVs are the series and parallel design, but other designs do exist. The series drivetrain had the EM running off the battery pack and the ICE converting chemical energy to electrical in series to supply power for the electric traction motor.

While the parallel drivetrain allowed the creation of propulsion from either the EM or ICE. The last type of EV are PEV, they were identical to the plug-in hybrids with the exception that they cannot be charged from the grid and they could only operate using the battery system. EV markets were being driven by battery technology and the factors of consumer interest, technological advancements, and cost improvements.

A detailed discussion will take place on the fundamentals of a battery because acceptance of EV requires knowledge of its core technology. Specific topics that will be examined are the principles of an EC cell, types of primary and secondary batteries, chemistries, safety of ABs, limitations and lifetime of batteries.

1.1 Fundamentals of a Battery

An EC cell had been the basis for modern EE storage since Alessandro Volta designed the voltaic pile. EC cells had the ability to either produce or storage electrical power when the cells are activated. This worked when chemical reactions in the cell generate EE or when EE were sent back into the cell to create a chemical reaction. Depending on the HC, reduction or oxidation occurred and continued to happen until the cell obtained a state of equilibrium state [5]. Optimal EE were achieved when two HCs with opposite potentials were joined to form one system.

Parts that make up the system were an electrolyte, a divider, and two electrodes. Anodes were electrode materials that had a negative potential and oxidized while cathodes are positive electrode materials that reduced during EC reactions. The potential difference between the anode and cathode formed the cell potential which could be called the NCV. This potential determined how much energy the cell would produce during chemical reactions. Larger NCV were highly desired because they generated more energy compared to lower NCV. The electrolyte could be the same or different material already used in both HC, but the electrodes ideally needed to be different materials to produce a potential difference.

There were limitations to the size of the NCV because there were limits to the potential of existing elements. Alternatively, a higher NCV could be established when EC cells were connected in series and in parallel. This new formation was called a battery; a battery consists of at least two EC cells. The term battery has been commonly adopted for a single cell even though battery means multiple cells. There were no major differences between a battery and an EC cell other than a battery has the ability to produce higher energy and power capability.

Two main types of batteries were primary and secondary systems. A primary battery was an irreversible system which only operated a single time generating EE until the battery's equilibrium was attained [6]. Once depleted of its electric potential, the battery had no use and should be recycled or thrown away properly. Some useful benefits of primary batteries were lower initial cost, expendable, easily replacement, lighter, smaller, long service life per charge, and good charge retention. A secondary battery on the other hand had the ability to be used multiple times due to the chemistry of the battery allowing reversible EC reactions [6].

These reactions occurred when EE directed into the battery caused a reverse in the EC reaction which almost brought the battery back to its original state. The recharging of the battery to its original state reduced the effects over time because the chemical reactions slowly created impedance on the electrodes preventing a full recharge. Secondary batteries were favorable when the battery could be used over a long period of time and

allowed the battery to have a lower life cycle cost. They also provided high discharge rates for high demand power applications, and secondary batteries exceled as emergency power systems. Primary and secondary batteries balanced each out by having the opposite strengths and weaknesses of each other. Batteries did not define the application rather the application defined the type of battery needed and knowledge of the types of batteries supported proper decision making for the system.

1.2 Chemistries

The main factor that decided NCV was the chemistry involved in the cell such as the electrode and electrolyte material. Cell chemistry played an important role in the safety, environmental impact, cost, cycle life, and capacity of the battery being produced. The discussion below will be divided into types of primary and secondary cell chemistries. To begin with, a couple of primary cell chemistries were the ZC battery (Leclanché dry cell) and the alkaline battery. The ZC cell used ammonium chloride as the electrolyte, zinc as the anode and manganese dioxide as the cathode [7].

Advantages to the ZC cells were cheap materials, suitable for primary battery operations, cost effective cell design and easy construction. Downfalls to ZC batteries were higher chances of battery leakage, low energy density compared to other primary batteries, short shelf life and poor performance in cold temperatures. Similar to ZC batteries, alkaline batteries had the same anode and cathode, but differed with a potassium hydroxide electrolyte [8].

Benefits of alkaline batteries were long shelf life, decent energy density, thoroughly researched chemistry and wide availability. Its unfavorable aspects were comparable to ZC batteries with poor high load behavior, and prone to leakage over time.

These battery chemistries represented the strengths and weaknesses of primary batteries. Primary batteries were good for small load, high energy, low cost, and temperature applications. A few secondary cell chemistries that will be discussed such as Pb acid, NiCd, NiMH, and Li-ion [6]. Pb acid batteries were built with lead plate for the anode, lead dioxide for the cathode, and sulfuric acid as the electrolyte. Some advantages of Pb acid batteries were their reliability, resilience against abusive handling, low internal impedance, long shelf life, and being made of inexpensive material.

Pb acid's shortcomings were the toxicity of the substance, very low energy density, short cycling, mediocre performance at extreme temperatures, and poor fast charging [9]. When analyzing NiCd chemistry with Pb acid, NiCd had a longer cycling period with appropriate maintenance, better temperature performance, extremely good fast charging, larger energy and power density. The unfavorable effects of using NiCd chemistry were the cell memory effect, and the lethal element of cadmium. NiMH chemistry could be seen as the brother chemistry of NiCd because they were closely related in performance and chemistry. They differed as a result of the anode being a different metal which allows NiMH to have a higher capacity, they were environmentally friendly, and they did not suffer as much from the memory effect.

The limitations of NiMH were the low cycling if repeatedly discharged to the maximum capacity, a higher self-discharge compared to NiCd, and a complex charging procedure. The main tradeoff for Li-ion were the requirement of a costly management system to prevent dangerous situations and a high initial cost for the battery. These conditions could be overlooked due to the fact Li-ion had an immense cycle lives that offset the cost, low capacity fade at different C-rates, a long calendar life, possible safer chemistries and the highest energy and power density [9]. Furthermore, LIBs could be designed allowing them to achieve high energy, power, or a mixture of both for a variety of applications whereas other chemistries cannot be designed feasible the same way. Out of all of the secondary battery chemistries, Li-ion appeared to be the most suitable battery chemistry for EVs.

1.3 Safety

ABs faced a wide variety of dangerous instances and as of now, the fundamental safety tests were based on extreme cases rather than a standard. Since there was not a unified standard for AB, most of the experiments discussed were similar to stationary and portable testing. Although batteries were being tested this way, they could be considered applicable due to the severity of the application, the battery chemistry, and the high tolerances for the test. Two recently new publications evaluated the safety of Li-ion in hazardous mining sites which could be related to AA [10,11]. The experiment had two parts, one part used the UL 1642 standard which focused on testing small replaceable lithium cells and the chances of fire or explosions.

While the second part was an altered version of the UL 1642 standards with the except of analyzing the battery during a crush and puncture test using a 90° plastic wedge. Small Li-ion cells should act the same way as large cells because they share the same chemistry, thus these experiments should be considered acceptable for AB testing. The batteries were tested in a chamber to control the environment such as inserting moderate level of methane, and varying the temperature from room 21-40 °C [10,11]. This allowed the collection of temperature, pressure, and other environmental changes for accurate results on finding the safest chemistry. These observations were carried out as a null hypothesis test and setting the level of probability that a pass or fail would happen was possible due to the setup configuration.

Tests revealed that the A123 26650, LFP cell chemistry, were a safer cell design compared LG Chem ICR18650S2, LCO. It also demonstrated that LFP had the ability to resistance substantial abuse without producing an explosion or fire while LCO could not. Between both chemistries, LFP appeared to be superior for safety and could be a possible candidate for AB applications. Another publication looked at the performance of various types of Li-ion cylindrical cells such as LFP, LMO, and NCA and their levels of safety [12]. The batteries being tested were all likely contenders for being adopted as an AB, but LFP had been the only chemistry that had been proven to be safe so far.

It was interesting to note that the investigation was done with cylindrical designs rather than prismatic. Cylindrical cells would be the ideal choice in AB system because the design provided higher structural integrity and maintained high performance levels. LIBs

designed this way were affected by the forces of stress waves and inertia during high and low impact scenarios [13]. The angle and position of the impact greatly affected if the LIB fails as well as the size of the battery during a bending situation. The first section of the research was to test the capacity loss at varying C-rate rates during and note if there was any heat produced during the cycling.

Zaghib *et al* wanted to identify what C-rate created the worst energy degradation of the cell. A crush and nail penetration was conducted to see if any thermal runaway or internal shorts were made. ABs would face a higher chance of being crushed or penetrated by an external object which was why the results of this test mattered in determining the safest chemistry for AAs. The conclusion of the publication was LFP provided outstanding safety and EC performance while other Li-ion chemistries lacked safety [12]. These experiments could be related to how well an EV would react during a car crash and the extreme level of safety LFP achieved.

Larsson *et al* analyzed the safety of LFP during a fire by looking at the variables of SOC, and the amount of toxic gas released [14]. The cases were set up using LFP mechanically united with wire over a gas collection system and single burning item system. Thermocouples were placed at various points on the battery pack, battery packs were charged to different SOCs, and the calendar life of each pack varied. Results revealed that batteries with higher SOC provided more combustible fuel the fire could consume to create a more volatile reaction.

It was also concluded that lower SOC gave off higher amounts of toxic gases and the level of gas produced from an average LIB pack for a PHEV would be higher than acceptable standards. After viewing the publications above, it was clear that LFP provide similar EC performance as other Li-ion chemistry while leading with superior safety. This was why LFP should be chosen as the best choice in designing a battery pack for an AA. Safety was a paramount concern when designing for a vehicle, but the inherent lifetime and limitations of the battery need to be taken into consideration.

1.4 Limitation and Lifetime of Automotive Li-ion

Automotive makers were interested in the limitations of EVs and these limitations stem from the AB. The battery pack had to be able to maintain energy and power performance during every day handling and still be functionary until the end of its lifetime. Energy fade illustrated how long a battery would last during a single charge as in day to day handling and power fade determined how long the battery's life would last. A publication sought to discover the effects of cycle degradation on LIBs [15]. The experiment consisted of using a prismatic LFP battery at a 3C rate and after every 300 cycles, characterization was done.

The LFP were inspected of capacity fade, power fade, pulse C-rate charge and discharge. Additionally, an UDDS was assessed at different temperatures during these 300 cycle intervals to check the performance of the LFP for EVs. There was very low capacity and power fading in high temperature environment initial until batteries were cycle further than 600 cycles.

LFP batteries obtained greater losses in capacity and power fade when being used at lower temperatures. Another publication evaluated how LIBs and Pb acid based batteries would behave for EV and HEVs [16].

Li-ion chemistries being implemented in the experiments were LFP, NCM, and Pb acid. Capasso *et al* ensured cases were comprehensive and analyzed how each chemistry would react to a real EV drive cycle. To create the realism, an urban scooter, an eddy current break, and uniquely designed flywheel were incorporated road resistance and vehicle inertia. The outcome of the experiment was that Li-ion performed superiorly to Pb acid chemistry in which it maintained exceptional voltage profile, capacity, and obtained a longer driving range. Groot *et al* did a study on the complex ageing of high-power LFP batteries at varying C-rates [17].

They came up with six different cases to study the battery with different variables. The first three cases were done to test symmetrical C-rate cycling with a varying temperature range, so there could be an understanding of how LFP was effected by temperature. Case four was carried out to test symmetrical cycling at numerous SOCs during high temperature. This would give insight on how the SOC effects the life of the battery. Furthermore, case five was to the effects of the rest period before battery use and the last case was asymmetric cycling at varied temperatures.

The outcome of the experiment was a strong correlation for LFP ageing at high temperatures, and high symmetric C-rates at full SOC. The amount of rest for the battery

was proportional to ohmic resistance, and dependent on cycling conditions. A rest period at any SOC or temperature was concluded to be bad for the battery. Also, asymmetric C-rates were seen as detrimental to the SOH to the battery. The optimal settings for a LFP battery was a low SOC, a small rest period, and symmetric cycling to improve the life of the battery.

The overall conclusion was that LFP chemistry was greatly reliant on temperature and SOC, but the chemistry could reach long calendar lives [18]. Li-ion chemistry could be as high as 8000 cycles at room temperature and attain low power degradation over a long time period while running EV drive cycles. Capacity fade would be the cause of EV driving range loss rather than power fade. Even though LFP had some flaws, it was the preferred choice for EV designs and it would be used as the battery for the experiment.

2 GOAL OF EXPERIMENT

The goal of the experiment was to check the performance of a LIB pack for a HEV using electric only driving in the city, and to determine the effects of driving in hot and arid conditions. Two test setups ran in tandem in the hopes of simulating these conditions for two different modes an EV would operate. The two driving conditions being looked at were a depleting and sustaining mode of operation. Many HEVs used a combination of both modes when running which a fully charged EV ran solely on the battery until a certain SOC was reached. This portion of driving would be called the charge depleting mode while a charge sustaining mode would use the battery in conjunction with the ICE.

The immediate focus of this experiment would be to determine the effects of a charge depleting mode, compare the results of both drive modes, understand the effects of a city drive cycle employing a charge depletion operation, and create a model for the charge depletion driving pattern. To measure the performance of the pack, the variables of capacity and power fade were chosen. These variables were picked because the amount of energy and power a battery could produce over a period of time seemed to be the logical choice of how to define performance of a battery. Data could easily be collected over a long period of time, and the data could help form a model to be used by others. There were many choices of potential models such as EC, mathematical, and EEM, but an EEM was picked.

The model had the ability to recreate capacity and impedance at specific cycles with the possibility of providing trend information. Trend information could be derived from the elements that made up the EEM and what chemical reactions they represented such as ohmic resistance, charge transfer reactions and mixed diffusion [19]. After deciding on the model, a driving schedule and a battery pack configuration was required to test how an HEV under electric only mode would handle during an ordinary day of driving. The US EPA UDDS was chosen to represent the drive cycle of a HEV because it simulated city driving patterns and the cycle could be converted into a current profile. Additionally, the derived current profile was adjusted to a charge depleting drive mode of seven percent regenerative braking to simulate the HEV relying primarily on the battery for momentum.

The battery pack arrangement was selected to be a single cell connected to another cell in parallel to prevent any cell discrepancies. This pack configuration would allow the cell model values to be divided in half, so the pack could be aggregated with a single cell or the pack itself. A detailed discussion on the selection of cell modeling, battery pack modeling, and drive cycles will be done to highlight why the above choices were made.

2.1 Cell Modeling

The demand for accurate and precise modeling of battery pack characteristics had been a high commodity because EVs were trending in the automotive market. It would be valuable to determine a method that was both efficient and accurate using only sparse resources. Cell models were the basic structure when it comes to designing any battery pack, and two methods of designing the cell model are the EC and behavioral model [20]. The EC model would be developed from the fundamentals of thermodynamics, kinetics, and transport phenomena of the cell's electrodes and concentrated solution [21]. This model took into consideration the conservation of mass and charge of solid and liquid materials and defined partial differential equations to represent the principal physics to form a Bulter-Volmer kinetic expression [22].

The expression was discretized into a set of algebraic equations to reduce the amount of time needed to run the model in a computer or battery management system. Advantages to this model were the comprehensive details of the battery structure and material being used. Its disadvantage were the huge amount of computational power and time needed to produce the model.

The behavioral model could be broken up into two subcategories which were the mathematical model or EEM [20]. A mathematical model was formed using collected data and curve fitting the data through an optimization algorithm or linear regression method.

Some methods of optimization algorithms include the Kalman filter, Levenberg-Marquardt, Powell's method, and Newton's method [23,24]. When using the mathematical model, it would be critical to remember that they were very fast in comparison to the EC model, but at the cost of accuracy. The EEM approach was created by John Edward Brough Randles on the same theory of the Bulter-Volmer kinetic expression used in EC model [25-27]. EEM was established using EIS to find the impedance of the cell by producing a small AC sine wave at varying frequencies. Electrical components portrayed the impedance of the battery at the tested frequency range and the accuracy of the model was determined by how close the model could recreate the impedance curve.

An added benefit to the EEM was the electrical components could express the faradaic and non-faradaic reactions within the battery and show possible chemical trends. A faradaic process was represented as a proportional relationship between the chemical reactions in an EC system and the amount of current passing across an electrode. While a non-faradaic process was the construction of an electric double layer using electrostatic principals to form a layer of a positive or negative charge between the electrode and electrolyte.

The three electrical elements adopted for the EEM also called the Randles circuit were two resistors and a capacitor. The resistor in series with the parallel connection of the other two components signified the ohmic resistance running through the electrolyte, electrodes, and the contactors.

The capacitor exhibits an electrical double layer capacitance being formed on an electrode or separator [25]. While the last resistor reflected the charge transfer resistance of the chemical reactions in the battery pack. This underlying structure of the Randles cell could be modified by adding additional parts such as CPE, Warburg impedance, extra RC networks, or other circuit components. Improved accuracy of the Randles circuit model could be achieved by adding additional RC networks for low and mid frequency impedance values or by defining more complex circuit designs. A CPE was an EEM component used to simulate a double layer or coating capacitance within a battery and the device could be considered somewhere in between an ideal capacitor and resistor [28].

This could be determined by finding the angle produced from an impedance curve on a Nyquist plot. An ideal capacitor would create a phase of 90° for its impedance curve while a resistor would not have a phase which results in a phase anywhere between 0-90° for a CPE. A specific case for a CPE could be considered as Warburg element which was used as a EEM element to show diffusion reactions within a battery [29]. The difference between a Warburg element and a CPE was a Warburg element had a constant phase of 45° for its impedance curve while a CPE does not necessarily have a 45° phase.

The EEM lied somewhere between the EC and mathematical models due to accuracy, resources needed, time, and complexity. One model was not completely better than the other, but it all depended on the scope of the project. Out of the three models, the EEM was highly favored because a reliably accurate model of the cell's AC and possible chemical response could be produced with limited supplies and time. Accuracy of this model could be found by calculating the coefficient of determination between the model and raw data values.

2.2 Pack Modeling

Once a suitable cell model was picked, the appropriate technique was chosen for the type of pack model that would be developed. The pack model could be designed to make a comparison between real time data and a model to obtain the SOC and other variable estimations [20]. Or the pack model could be used to help battery designers create a pack for a specific application such as a EV battery. These techniques were dependent the amount of detail put into the cell and the pack model being incorporated. Three options to fill either of these roles were the aggregated cell, scaled cell, and well-known battery pack models.

The aggregated cell model duplicated the cell multiple times with series connections to increase the pack voltage while parallel connections could be done to increase the capacity. Both procedures would be done until the desired battery pack voltage and capacity was obtained. This approach required the least amount of effort while maintaining a considerable amount of accuracy for the cell design. The major downside to this model

was it does not take into consideration cell variations, thermal unbalancing, and other variations that could occur in a cell. A second option could be scaling the cell model to the size of the desired battery pack after figuring out any cell discrepancies that would occur in the chemistry for any situation [20].

This produced a simplified and thorough pack model that could be simulated rapidly on a computer, but this pack modeling required a large amount of time and resources that were sometimes not available. The third choice of modeling relied on using a well-established battery pack with the ability to cover any circumstance the pack would run into during operation. For this method to work, the cells in the pack had to be well balanced during any case as well as controlling the proper temperature. The benefits to this modeling process were the cells inconsistencies and thermal impacts were already incorporated into the model which allows for fast simulations. An aggregated cell model seemed to be the logical choice out of the three pack models because it demands the least amount of effort in regards to resource and still preserved accuracy with a properly selected cell model.

2.3 Powertrains for EVs

When it came to designing PTs for EVs there were many different options to choose, but the types of architectures for EVs were PEVs, series, parallel, and power split PTs [30]. PEV PTs had two classifications which were an EM, and a EM with a gearbox. The EM only design had the advantages of high speed range with no gears, large torque capability at low speeds, and the simplicity of the design.

An EM with a gearbox PT balanced the shortcomings of the previous design of single speed efficiency drops, but this required a more complex design. HEVs had a copious amount of PTs and depending on the architecture it effects the classification of the HEV.

The micro hybrid would to be first designation of a HEV PT vehicle which used a parallel scheme of an ICE in parallel with a EM connected to the transmission [31]. Features of a micro hybrid were mentioned before, but the downside to this PT was the lack of PEV driving option. The mild hybrid PT compared to the micro hybrid had the additional benefit of regenerative braking due to the EM being mounted between the engine flywheel and transmission of a parallel design. A third type of parallel PT architecture incorporated a EM before or after the transmission being linked to an ICE. This PT would be used in a mild, full HEV, and PHEV due to the nature of being able to function like the previous PTs mentioned as well as having the ability of a PEV drive mode.

A second option for HEV were series PT which had less layouts due to the nature of the PT and the parts involved with locomotion. The basic form of a series PT was an ICE running a EM that supplied power to a traction motor or a battery pack supplying power [31]. This design allowed the ICE to operate at optimal efficiency, a reduction of mechanical conversions within the architecture, and large amount of torque generation at low speeds. Its downsides and the reason this PT were not used that often were multiple energy reductions during efficiency conversions. There needed to be a high quality traction motor in this design otherwise there would be a loss of locomotion during extreme loads.

The last type of PT available to HEVs were the power-split variation which mixed series and parallel PT. Three optional forms were an input-split, an output-split and an input-output split design [30]. An input-split required the ICE and two EMs to be linked to a power-split device, and the output-split had the same format except one of the EMs are joined directly to the ICE. The input-output split also called a compound-split required multiple power split devices interconnected and a greater complexity in design. Each power-split PT design were very complex in nature and provided varying efficiencies at different operating conditions.

The main characteristics of the power-split design would be defined as how the torque was produced and what driving mode gave the best performance. The torque provided to the engine could be divided into the ICE or EM delivering the necessary power and the efficiency was defined as the speed and torque required. As the complexity of design increased for HEV PT, so did the cost and efficiency of the vehicle generally. There were advantages and drawbacks for every PT architecture, but the performance of the vehicle would be dependent on the operating conditions.

2.4 Drive Cycles

Originally, drive cycles were created to test the emissions of mobile sources in the country which could be divided into two categories, on-road or non-road vehicles [32]. Those categories could be broken down into subcategories for all the different types of vehicles such as light-duty vehicles, heavy-duty vehicles, locomotives, aircrafts, and many other modes of transportation. Drive cycles were usually investigated for any type of vehicle

from the category by placing them on a dynamometer and following the proper schedule [33]. Measurements of carbon could be collected from an experiment like this to figure out the fuel economy while EVs required a different method of testing. To test the battery pack performance in EVs, drive cycles in the light-duty subcategory were adopted and converted into current profiles [34].

A light-duty vehicle was a passenger car or light truck that the average person would own and therefore would be the leading choice of drive cycle types for EVs. The light-duty subcategory had five drive cycles and most of these driving schedules were modified to current profiles to simulate driving conditions of an EV. These five drive cycles were the US06, HWFET, SC03, FTP-72, and the FTP-75 [32]. The US06 SFTP symbolized aggressive driving patterns with higher speeds and large accelerations during the schedule. The HWFET or HFEDS provided a driving pattern that emulates mild driving on the highway under 60 mph.

An air conditioned drive cycle called the SC03 SFTP was utilized to emulate how a vehicle using the air conditioner while driving adds a higher load on the engine and emissions of the vehicle. The FTP-72 also called LA-4, FUDS, and UDDS was conceived to match the driving pattern of city driving [35]. FTP-75 was almost identical to the FTP-72 with the addition of an extra 505 seconds of the UDDS to mimic the car driving with a hot engine.

Out of the light-duty vehicle driving schedules, the FUDS was chosen to represent the driving conditions in a hot and arid environment. The FUDS drive cycle profile was normalized from physical power to electrical power, so the velocity of the cycle could be converted into a current profile that would be used by an EV [34].

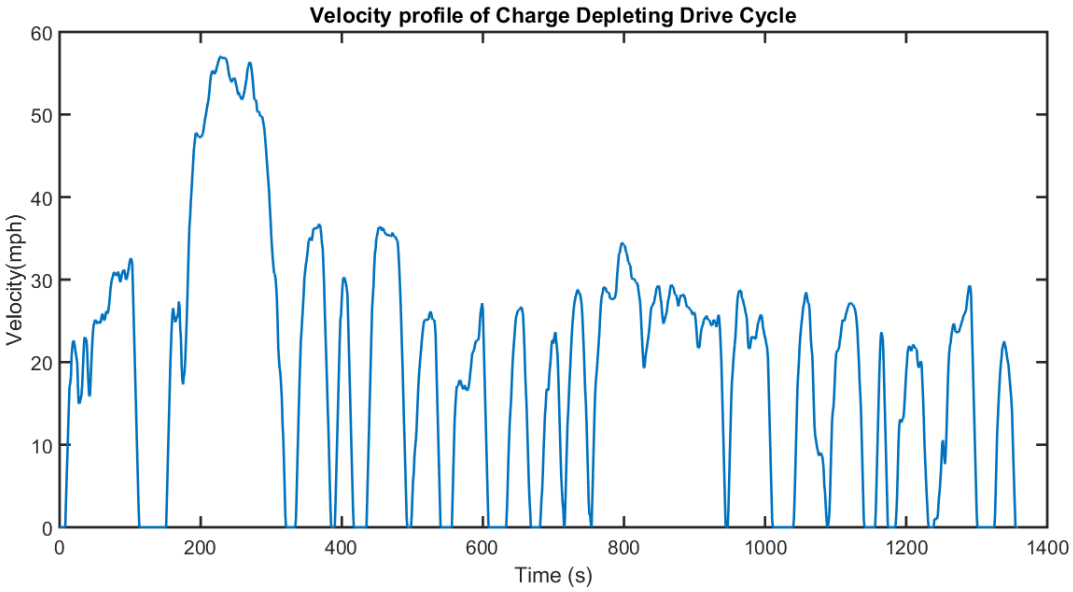

Figure 1: FUDS Charge Depleting Velocity Profile

Four factors that affected the conversion are the acceleration, incline of the vehicle, rolling resistance, and aerodynamic drag factors [36]. EV driving conditions were considered to be flat, had smooth wheels, and were driving in very hot temperatures, thus removing every factor except acceleration on the conversion to current. The nomenclature used for the current profile was positive current values signified that the battery acquired power while negative current indicated current was given. Velocity was altered to acceleration by finding the different between the future point and preceding point then divided by time. This value was multiplied by the maximum current of the battery testing equipment divided the maximum acceleration to receive a current value.

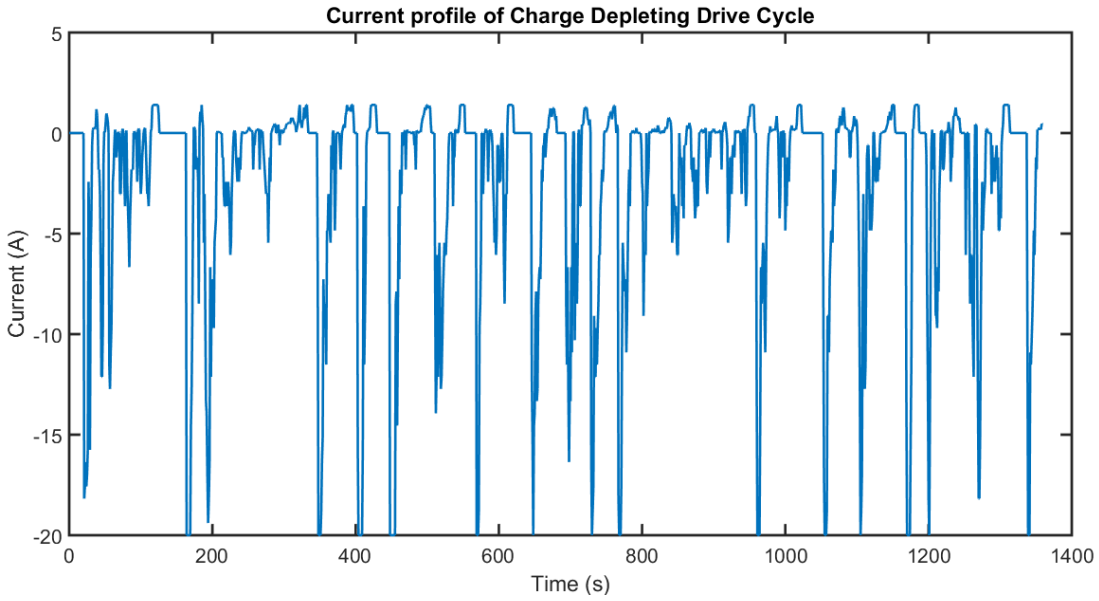

Figure 2: FUDS Charge Depleting Current Profile

If current was greater than zero, current values were multiplied by seven percent to reflect the amount of energy restored by regenerative breaking. The results of this transformation were called the FUDS charge depleting current profile and it was the profile used to simulate the charge depleting drive cycle for the HEV. It was worth mentioning that the charge sustaining drive cycle used in the experiment was a modified version of the FTP-75. The charge sustaining drive cycle was based off the inertia, torque, and velocity equations of a 2005 Chevy Equinox driving a FTP cycle [37]. It had a parallel through the road PT that ran the ICE at high speeds from the front drive and the EM at low speeds from the rear drive.

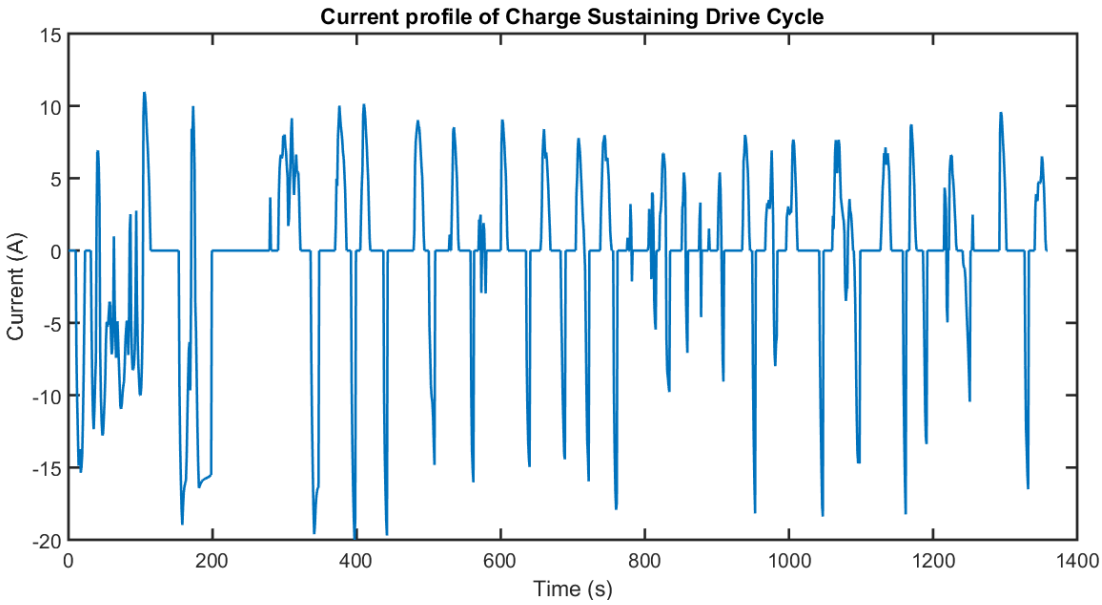

Figure 3: Modified FTP Charge Sustaining Current Profile

3 EXPERIMENTAL SETUP

The experimental setup had two battery packs running simultaneously with two different drive cycles in different temperature conditions. The primary equipment was the Arbin BT-2000, model BT-M-40, a battery testing station. Arbin was the premier choice when it came to battery testing and it could be seen as a standard for testing batteries in the scientific community which was why it was chosen [38,39]. The specific model had two channels that could run independently of each other and send a variety of voltage, current and drive cycle profiles. The voltage and current range limit for each channel was 0 - 40V and -20 - 20A.

A voltage range limit of 2-3.6V and a current range limit of -20-20A was established to ensure the safety of the lab, the battery packs, and the battery testing equipment. A testing oven was used to control the temperature for the battery packs to simulate a hot

and arid setting. The oven was a Thermo Electron Corporation: Precision oven which could create the desired environment for the batteries. The oven produced a dry heat through convection and periodically, LIB packs were analyzed with EIS using the Parstat 2273 to find the impedance of the cells during its current cycle. The Parstat 2273 was a galvanostat and potentiostat that could perform EIS by using a single sine wave method [40].

This method worked by setting a constant amplitude and varying the frequency of the wave being injected into a battery. As a result, it produced a Nyquist plot showing the battery's impedance throughout the frequency range. Any inductive and capacitive material would give an increase or reduction in impedance depending on the frequency and material the signal went through. The voltage, current and frequency range of the instrument was -10 - 10V, -2A - 2A, and 10μ - 1MHz. Battery packs were connected with a counter electrode and reference electrode lead at the anode while the working electrode and sense electrode lead were connected at the cathode.

This allowed the Parstat to properly take impedance readings of the battery using the software PowerSuite which had several subsections. The single sine wave method was operated from the PowerSINE section of the PowerSuite software. LFP cells 26650 were purchased from a reliable manufacturer to form the battery packs in the experiment.

Each 26650 cell had a nominal voltage of 3.6V, a rated capacity of 2.5 Ah, and a high rated cycle performance with a large C-rate possibility. The composition of the battery pack contained one cell in parallel with another cell to maintain the nominal voltage and to double the capacity of the pack.

It was desirable to increase the size of the LIB packs to have a high C-rate, but an increase in pack size was limited to prevent damaging the Arbin and Parstat equipment. LIB packs were thoroughly covered with electrical tape to prevent any short-circuits or unintended contact. Both LIB packs were initial placed on a portal dolly with a wooden platform to provide electrical isolation. This was done to give a base reading on each LIB pack to see the performance under normal room temperature and nominal air moisture conditions. Eventually, both LIB packs were placed in the Thermo oven with thick pieces of plastic to preserve electrical isolation as part of the experimental procedure.

3.1 Experimental Procedure

The desire of the experimental procedures was to test batteries at two different temperatures and drive cycles. Temperatures that were being used were room temperature of 25 C° and high temperature of 50 C°± 2C°. Experimental procedures were done through the Arbin battery cycler and the MITS Pro software that ran the equipment.

MITS Pro was an easy to use interface and logic driven software that allowed multiple channel to run independently of each other. It gave the ability to control, monitor, and record raw data from an external source that was being tested as well as the option to modify the program while running in real time.

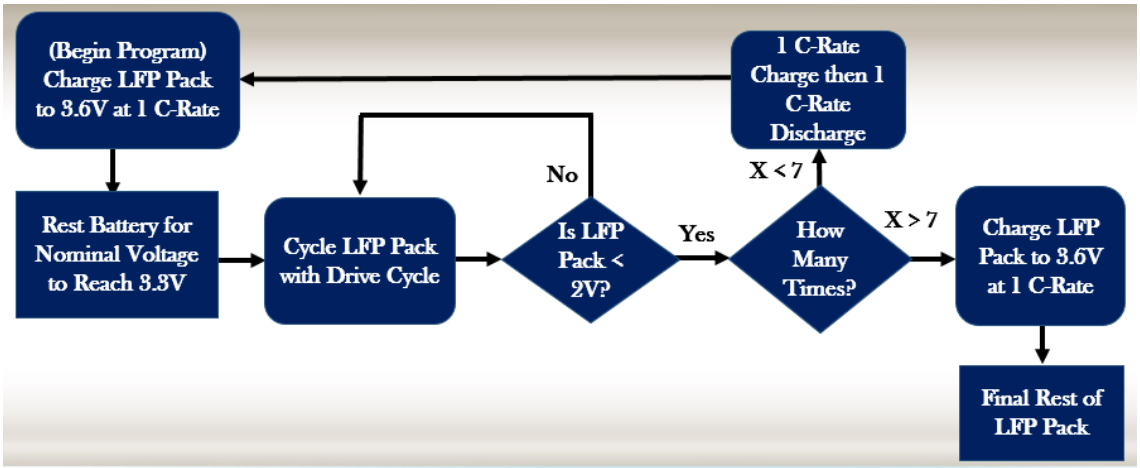

Figure 4: Flow Chart of Battery Testing

Two programs were created with similar structure for the program, but differences occurred for the current profile being implemented. The charge sustaining current profile ran for 1360 seconds and the charge depleting current profile ran for 1370 seconds. Three major sections of the program were the initial charging of the battery, cycling the battery until hitting the SOC limit, and a constant charge and discharge stage. A single cycle in the experiment was considered to be anytime the pack was charged, discharged, or running the HEV current profile. Initially, both LIB packs ran for ten cycles at a constant C-rate of one for a charge and discharge phase to check the batteries preliminary capacity.

Afterwards, battery packs were cycled for roughly 50-60 cycles in room temperature to get a base reading and the rest of experiment had the batteries cycling at 50 C°. The battery packs were initial charged at a one C-rate until the pack voltage reach 3.6V while collecting data every ten seconds. Then the packs rested for five minutes to ensure the LIBs were fully charged before testing under a drive cycle and to let the nominal voltage return to 3.3V. Next, LIB packs were continually cycled under a current simulation mode in MITS Pro that ran the current profile of the drive cycle. Data was recorded every one second until the battery pack reached 2V.

It would usually take five to six drive cycles of charge depleting mode to discharge the pack to 2V and roughly 19 drive cycles to deplete the charge sustaining profile. Once 2V was reach, packs would be placed into a constant charge, a rest of five minutes and then constant discharge at a 1 C-rate while collecting data every 10 seconds. Then the LIB packs would go back to the first stage of the program of being charged at a 1 C-rate and the pack would go through the same steps again for a certain set of cycles. The charge sustaining profile battery pack would run through the entire program roughly five times to discharge the LIB pack to the SOC limit and the charge depleting would run its program approximately seven times. LIB packs ran this program to cycle the charge sustaining pack for 283 cycles and 1007 cycles for the charge depleting pack.

Periodically during drive cycle testing, batteries would be fully charged to 3.6V and tested with the Parstat 2273. The settings for the EIS single sine wave test was a 50mV amplitude and a frequency range of 1k-10mHz.

This was done to check the impedance fade of the LIB pack over the cycling period while the Arbin recorded data for the capacity fade. Capacity fade data was taken during the constant charge and discharge phase of the program. LIBs had a capacity rating of 5Ah, so capacity was found by taking the time the battery ran for charge and discharge and dividing the individual times by one hour and multiplying it by five. This gave the battery pack's charge and discharge capacity percentage left. This method ensured the collection of accurate results for the charge and discharge capacity fade of the battery pack.

4 DISCUSSION

The sections below will break down the experiment into several sections to discuss methods of the EEM and how results were obtained. The categories were the creation of an electrical modeling element, the establishment of the EEM, steps to collect data, modeling procedures, how a mathematical transfer function was made, and the accuracy through the experiment. This was done to illustrate the flow of the experimental design and to give a better understanding of the results obtained from the experiment. A major portion of time will focus on the EEM due to the importance and impact the model could have on future works. One of the major influence on the EEM was the collection of capacity and impedance data.

4.1 Data Collection of Capacity and Impedance

Two sets of primary raw data were collected during the experiment, impedance of the battery during a fully charged state and capacity of the battery during cycling. Initially,

capacity measurement readings for the battery were gathered every battery cycle to maintain high fidelity. Later, it was found out that the current profiles were being shifted slightly from the input of the Arbin system which would lead to error in the results of the experiment. This was due to the limitations of the Arbin battery cycler sampling time. To correct this situation, batteries packs were cycled from fully charged to discharged using HEV current profiles five times followed by the constant charge and discharge phase of the program.

Capacity was compiled during the constant charge and discharge phase of the LIBs because there were no transient effects occurring in that stage. MITS Pro recorded the amount of time in the constant charge or discharge phase which was divided by one hour and multiplied by the initial manufactured value of 5 Ah capacity to retrieve the true capacity of the pack. Packs were occasionally stopped and fully charged to take impedance measurements which took place every fifty to one hundred cycles. Impedance measurements were taken as much as possible, but the Parstat 2273 required maintenance several times throughout the experiment. Also, packs were ideally kept cycling on the Arbin to prevent cell relaxation and the effect it had on capacity and impedance fade.

EIS was done to packs once the system was stopped and the packs were fully charged. It was desirable to maintain 50 C° and a fully charged battery to see how electrochemical reactions in hot and arid conditions would be effected. A single sine wave process was used for EIS with the settings of a 50 mV rms amplitude and a frequency range of 1k-

10mHz. The frequency wave was selected based on capturing ohmic, charge transfer and diffusion reactions for the LIB packs. An amplitude of 50 mV rms was chosen because it was roughly 1.5% of the nominal voltage of the battery and to reduce noise interference. PowerSuite recorded the results of the EIS from the PowerSINE application and the data was converted into a text file for later calculations.

4.2 Inverse Constant Phase Element

The conception of the ICPE will be discussed, so there would be a better understanding when the modified EEM was explained. CPE were defined as a variable that could be somewhere between a resistor and a capacitor, but there was little to nothing mentioned about the equivalent version for an inductive variable [41]. A ICPE would be a user-defined element created to portray an element that was somewhere between a resistor and an inductor. Before going further in the explanation of an ICPE, a capacitor and CPE must be discussed in detail to understand the conception of an ICPE. The fundamental equation for a capacitor was current equals capacitance times the change in voltage.

To find the impedance of a capacitor the Laplace transform of the equation could be taken assuming all initial conditions are zero. The voltage signified the output and current served as the input which transformed into the inverse of the capacitance multiplied by a radian value. CPE had a comparable equation to the Laplace transform of a capacitor, but the CPE differed with the addition of the radian value being raised to a value of alpha [42].

The value could be anywhere from 0-1 which shifts the phase of the component to 0-90°. When the value of alpha was zero, it produced a resistive impedance while an alpha of one created a capacitive impedance.

A value anywhere in between 0-1 made an element in the forms of a resistive capacitor. Dhirde *et al* mentioned the use of modifying the CPE equation using a range of -1 to 0 for its raised power on the imaginary section of the equation to determine the phase [43]. This would give an opposite phase value that an inductor would have compared to a capacitive phase using a CPE with a raised power range of 0-1. ICPE takes a relatable approach as Dhirde *et al* by trying to achieve reverse phase adjustment, but the method used was to express it as an inductive equation. The fundamental equation for an inductor was voltage equals inductance times the change in current.

Complementary to the capacitor example, the Laplace transfer was taken for the inductors fundamental equation with the same inputs and outputs variables of current and voltage to find impedance. After finding that the impedance of an inductor was inductance times radians, the equation could be modified to invent the ICPE equation by raising radians by alpha. The range of alpha was now identical to the CPE range and the phase is -90-0°. It was important to note that either CPE or ICPE alpha range values could be extended beyond 90°, but a phase greater than ±90° represented an additional CPE or ICPE connected to the original component. The creation of this component was to fill the opposite role of a CPE, so the modified EEM could better match the Nyquist plots.

4.3 Modified Randles Circuit Model

The initial EEM considered as a possible candidate that could predict the capacity, impedance, and voltage profile of the LIB pack was a Randles circuit. It was seen as a frontrunner because it had the ability to match some of the raw cycle data characteristics from the Nyquist plots. A Randles cell had the added benefit of having a visual representation for chemical reactions occurring in the battery [44]. These visualizations could show the chemical reaction trends of diffusion in the electrodes, charge transfer reactions, coating capacitance, double layer capacitance, erosion of the current collector, and the effects of test equipment on the battery. The main issue with the Randles circuit was its ability to recreate a complex impedance curve due to the simplicity of the model.

Additional RC networks could be added to Randles circuit to improve accuracy, but the results of the model would not be the same as the raw data unless there were modifications done. Three variations in the Nyquist plots compared to the Randles circuit results was a loop formation between low and medium frequency as well as the phase being lower or greater than ±90° at the lower and upper frequency tails. To correct these irregularities, a CPE, an inductor, and a ICPE were added to the circuit model. The electrical circuit had an ICPE in series with a resistor which was in series with a parallel network. The components in series could be called the collector corrosion inductance and the ohmic resistance [45].

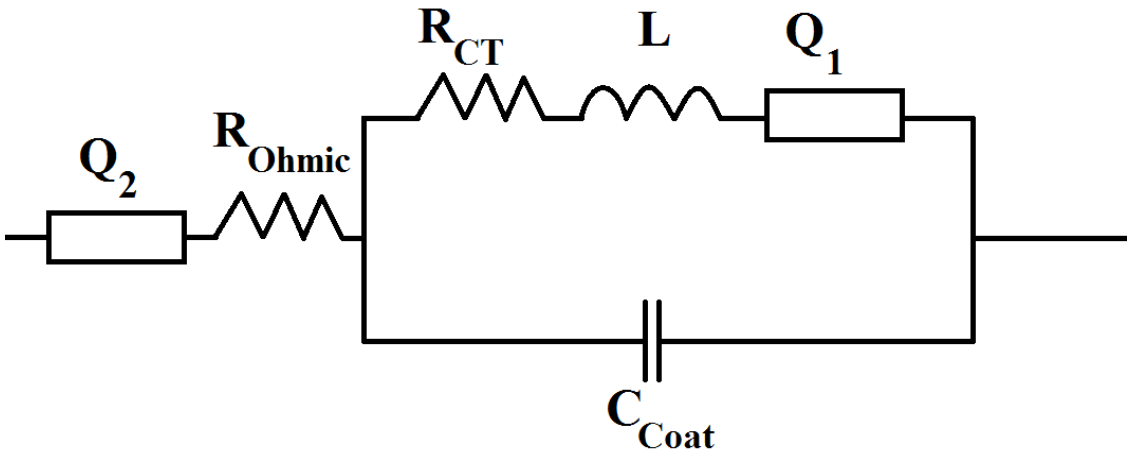

Figure 5: Modified EEM Circuit

An ohmic resistor expressed the trend in resistance for the electrolyte, electrodes, and the contacts of the battery. An increase in corrosion occurred on the electrodes, electrolyte, and contact material as the batteries are cycle which developed higher resistance. A ICPE symbolized the degradation of the current collector and the impedance added from the testing equipment [45]. The parallel network had a series connection of a resistor, an inductor, and a CPE in parallel to a capacitor. The resistor could be seen as a charge transfer resistance, the inductor as charge transfer inductance, the CPE as double layer capacitance on the electrode divider, and the capacitor as coating capacitance on the electrodes [46].

While the charge transfer resistance illustrated the electromagnetic and chemical reaction energy necessary to pull electrons from one material into another material [47]. This component showed the conductivity of the electrolyte and the speed of the equilibrium chemical reaction that happened between the electrodes and electrolyte. The charge

transfer inductance were possibly created from the formation of growth on material in the battery which would increase the length and area of the material [48]. This length and area expansion could generate higher inductive material when energized with current and could produce vibrations. Another source of inductance could be from the absorption of the electrolyte into porous anode or cathode material producing a larger dielectric and magnetic permeability [49].

A third conceivable option for charge transfer inductance was the nonhomogeneous concentration of material within the battery. Lastly, the CPE could conceivably be depicted as layer of electrons or LFP crystals forming on the plastic membrane divider to construct a double layer capacitance. Since the double layer was most likely not uniformed, it would not have a 90° phase like a capacitor and it would require an adjustment of its phasing using a CPE. The capacitor depicted the quality of carbon coating on the electrodes during cycling and how capacitance was effected during the pack cycling. Reaction representations of the CPE, ICPE, and inductor had several plausible electrochemical causes that were hypothesized, but additional research must be done to verify these results which could be done in future works.

4.4 Impedance Transfer Function and Capacity Linearization Procedure

The modified EEM and impedance transfer function were seen as a black box design during the experiment due to the lack of equipment to authenticate chemical reactions within the battery. This was not to say the model did not accurately embody the impedance values of the battery rather the lack of accuracy for the trends of individual

electrical components. The details of finding theoretical electrical circuit values were written below as well as solving for the modified EEM into a transfer function. An approach of transforming electrical devices before solving for the total impedance was taken, but circuit analysis using nodal or mesh analysis could be used to find the same results. The impedance transfer function was solved by finding the total impedance of the modified EEM and the use of the Laplace transform.

Individual components were transformed from the time domain to the s-domain using current as the input and voltage as the output of the Laplace transform. This conversion of output over input gave the impedance of each component which could be later used to combine with other parts. The total resistance of the entire circuit was the impedance of the ICPE in series with the ohmic impedance which was in series with the parallel impedance network. This parallel network impedance was defined as the impedance of the charge transfer resistance, charge transfer inductance, and double layer capacitance in parallel with the impedance of the coating capacitance. After mathematical rearranging in a transfer function form, the impedance transfer function turned out to be a fractional order function that changed with cycling.

An overall impedance transfer function was designed to incorporate the trend of each electrical part over pack cycling. This entailed solving the fundamental electrical circuit equations of the modified EEM for each cycle impedance data that was measured. Values for each electrical device went through regression analysis to find the best trend of value over pack cycling. The final result was combining the regression analysis

equation for each electrical component into the transfer function of the modified EEM to simulate impedance over pack cycling. To begin, recorded impedance cycle data was set between the frequency of 1k-240mHz to establish uniformity and the data was divided into three sections.

Section one was the high frequency tail that had positive real and imaginary data which represented inductive elements. The second region was the mid frequency segment that had the half circle in the negative real and imaginary part of the Nyquist plot. While the last chunk was the low frequency tail that had the negative real and imaginary values that defined capacitive components. The ICPE value was found in the first section where an inductive tail was shaped. Since the ICPE exhibited inductive qualities, the magnitude and phase of the impedance tail was taken at high frequencies to serve as the ICPE values.

A similar approach was done for the CPE at the low frequency range to solve for the double layer capacitance value. To get the values of each electrical element in the modified EEM, the ohmic and charge transfer resistance value of the EEM were required. Since resistance was not dependent on frequency, ohmic resistance was the x-axis value when the impedance curve initially crossed the x-axis at the beginning of the half circle. The charge transfer resistance would be the x-axis value where the other end of the circle crossed the x-axis minus the ohmic resistance. To identify the value of coating capacitance, the frequency at the maximum point of the half circle in the second section was required.

This peak in the half circle expressed an RC time constant between coating capacitance and charge transfer resistance. Thus, the coating capacitance could be found by multiplying charge transfer resistance times the peak frequency and inversing the value to find capacitance. The charge transfer inductance was found by looking for the frequency where the impedance curve forms a loop. This loop was formed between the low and mid frequency range of the Nyquist plot and it symbolized the resonant frequency of the material reacting to the single sine wave. Charge transfer inductance value was found by solving the LC time constant between charge transfer inductance, the frequency at that point, and the double layer capacitance.

Electrical values were optimized to improve the accuracy of the model after every device was theoretically found. Capacity linearization was done using the method of linear regression to give a first order equation of how LIB packs capacity faded over time. The linear regression equation could be transformed into a voltage source that changes over pack cycling, so it could be used in conjunction with the impedance transfer equation. Another benefit to the linear capacity equation was the percentage of battery capacity over cycling could be multiplied to the voltage profile to shift the profile over pack cycling.

4.4.1 Accuracy of Impedance and Capacity Modeling

To safeguard the accuracy of the impedance and capacity models, regression analysis was done in Matlab on the three sections of the impedance curve. This allowed the precise

collection of real and imaginary data as well as frequency when solving for electrical components. Outlier analysis was done on electrical values to remove any minor or major outliers to improve accuracy. The coefficient of determination was integrated as a filtering system during the optimization of electrical values and to demonstrate the quality of the final impedance and capacity transfer functions. This method helped maintain a high coefficient of determination throughout the calculation portion of the experiment.

4.5 Butterworth-van Dyke Circuit

Macia *et al* discussed that dynamic systems could be converted from a physical system into a mathematical model [50]. This conversion was done by categorizing sections of the physical system with proportional electrical elements. The electrical elements were connected in a way that would confer how the entire system was interconnected through series and parallel circuit combinations. This was another way to represent the physical system as well as giving the option to simulate the system using modeling techniques. The electric system could be converted into a transfer function with the use of differential equations and the Laplace transform.

The name of this approach would be the equivalent circuit method. This control engineering method allowed many different systems such as thermal, hydraulic, translational, and rotational systems to be simulated computationally. The modified EEM model created for the experiment took on the form of a BVD equivalent circuit which the circuit had been commonly used to design resonators from quartz, thin film,

and other piezoelectric material [51-53]. A BVD embodied the acoustic properties of a crystal in a resonator and correlates the acoustic impedances and loads. The RLC series connection within the BVD showed the effect of the mass and stiffness of the resonator while the parallel capacitance demonstrates the resonator at rest.

Some common applications that used a BVD circuit for resonator design were watches that use the crystal to keep track of time, a clock signal for digital electronics, and a frequency stabilizer for radios. The piezoelectric effect allowed certain materials to generate electricity when applying pressure or a mechanical force when applying voltage. These effects worked because the structure of the material was not symmetric and could create an electric dipole moment that formed an electric potential or mechanical force. Quartz crystals used this effect to resonant by applying a voltage potential to stimulate the crystal to oscillate at its natural frequency. It was important to note that many other types of material could resonate with the appropriate input because most material have a natural resonant frequency.

The original intent of the EEM was to find electrical impedance of LIBs, but additional information of finding the acoustic effects could be obtained. This meant the model could connect the electrochemical reactions with the mechanical effects and in turn produce noninvasive methods of determining the performance of LIBs. LFP material were typically considered an olivine crystal structure since synthesis required high temperatures and it was a mixture of lithium, iron, and phosphorous salts [54].

An olivine structures demanded high temperatures due to the nature of the Bowen's reaction series which illustrated the transformation sequence of mineral crystallization. Bowen's reaction series stated what temperature and pressure were needed to transform one stage of mineral into another.

This was broken up into two sections, the continuous and discontinuous reactions. Only the discontinuous reactions will be discussed because Olivine structures were a part of that section. The discontinuous reactions only developed the next crystalized mineral when there was enough silica with the pre-existing crystal and the correct temperature was held constant. A reaction would not occur if these requirements were met which resulted in the material maintaining the same structure. This was important to the synthesis of LFP batteries due to the fact that other crystalline structures could be produced in during synthesis and could change the performance of the battery.

The quality and concentration of LFP being developed may have variations of other types of crystalized material which may aid to the possible resonance LFP batteries. Gorzkowska *et al* experimented on the transition of LFP substance and found the presence of four different crystal forms of LFP [55]. One of the four crystals substances was a $LiFePO_4$ quartz like structure that could be seen as piezoelectric material. Dompablo *et al* found four substances during their experiment with $LiFePO_4$ which one crystal was in berlinite form, a $LiFePO_4$ quartz like formation [56].

These forms of $LiFePO_4$ were possibly generated from the delithiation of $LiFePO_4$ during the olivine stage at ambient pressures. An interesting aspect of this material was the structure transforms into an electrochemically inactive substance that could be monitored by the concentration of the crystallization. This monitoring could be done by checking the resonant effects of the material when using the modified EEM for EIS.

5 RESULTS

The results of the experiment showed that LFP packs using a charge depletion mode at high temperatures could last half as long as packs at room temperature. Secondly, LFP cells could maintain twice as much capacity and cycle for three times longer under a charge depletion mode compared to a charge sustaining mode. Also, the capacity fade of the charge depletion mode was marginal compared to the impedance fade of the battery. A 50% reduction in power of LFP batteries would happen 2.5 times sooner than 50% reduction in energy for the charge depletion mode at high temperatures. This meant that EVs would be able to preserve their driving range in high temperatures better than their towing and acceleration potential.

5.1 Cycling Effect on Impedance

LFP packs had no signs of cell imbalance, and the design of having two EC cells in parallel with each other gave the ability to divided the pack impedance values in half. The results in this section would be based off pack results rather than individual cells, but trends, values and impedance effects to cells still apply in the same manner. The initial impedance of the LIB pack running the charge depleting drive cycle was 4.171 mΩ and

the final value of 9.188mΩ was recorded at cycle 881. Cycling batteries at a high temperature and using predominately high C-rate current profile more than doubled the impedance of the pack. The LFP pack lost fifty percent of its power capability within roughly 900 cycles since the current and voltage profile were held constant.

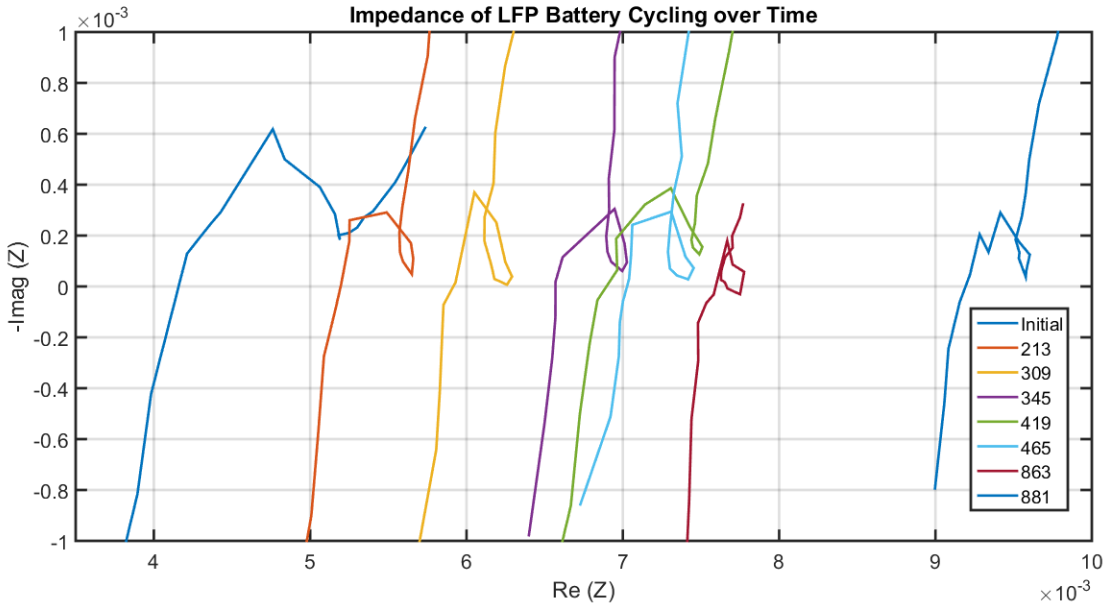

Figure 6: Charge Depleting Mode Impedance over Battery Cycling

This would be very concerning to the power performance life of the battery especially during long cycle periods. There would be a significant drop in power every 900 cycles under these circumstances. These results suggest that it would not be ideal to run LFP packs at high temperatures and large C-rates for a long period of time. Depending on the power application, LFP packs could deteriorate rapidly with these settings and the pack would not be able to meet the requirement of high powered systems. Regression analysis was done on the raw data to get the equation which expressed the LFP pack gained about 5.775μΩ of ohmic resistance every cycle.

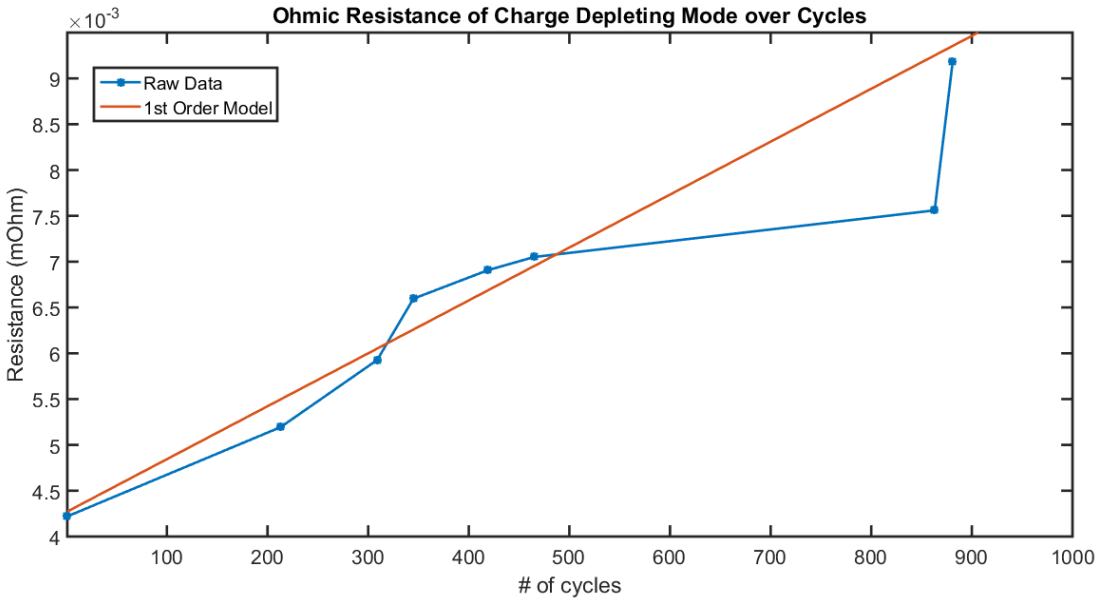

Figure 7: Ohmic Resistance of Charge Depleting Mode over Time

Cycling LFP pack batteries at lower temperatures or during less strenuous C-rates would improve the impedance fade of the pack. The accuracy of linear regression was checked by calculating the coefficient of determination of the data which was 93.6% comparable to the raw data. This would be an acceptably high value of accuracy and this value could greatly be improved with the collection of more impedance data. The results mentioned above were based off the raw data and linear regression model of the raw data.

5.2 Cycling Effect on Capacity

Initial capacity of the LFP pack being tested under the charge depleting mode was 4.998Ah and the capacity after sixty cycles at room temperature was 4.973Ah. Room temperature results showed that the batteries only lost a half percent of its capacity over sixty cycles. The LFP pack would lose only 0.412mAh for every cycle it ran the charge

depleting drive cycle at room temperature. This would mean the LFP pack would be at seventy percent of the pack capacity roughly after 3700 cycles if the linear trend of room temperature capacity continued. It would be safe to say that LFP cells have great cycle performance at room temperature.

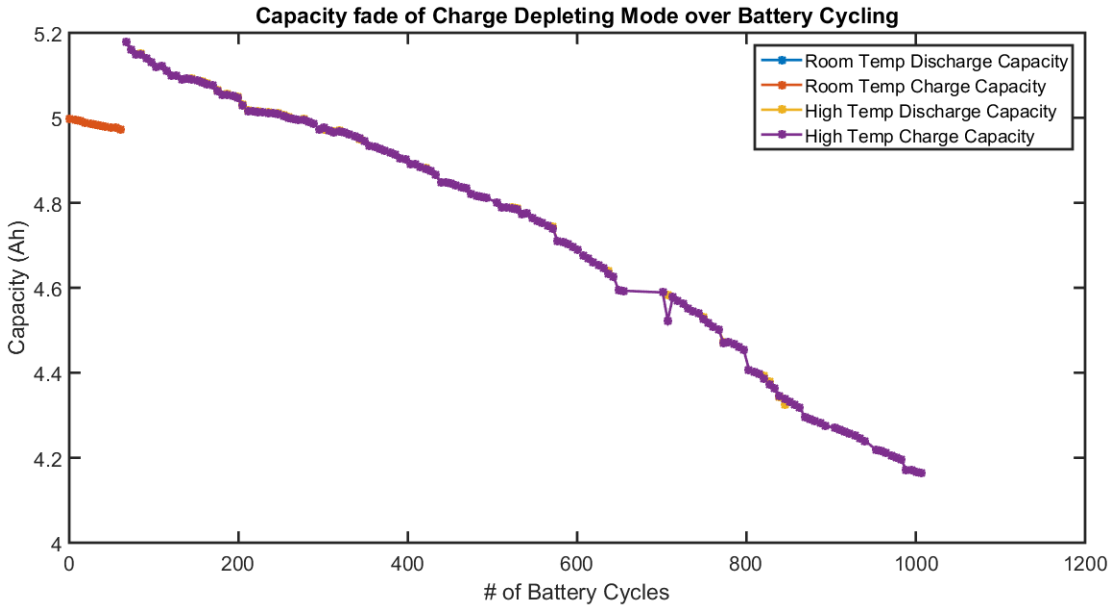

Figure 8: Capacity Fade of Charge Depleting Mode at Room Temperature and 50C°

The initial capacity at 50 C° using the charge depleting drive cycle was 5.179 Ah and the capacity after 1000 cycles was 4.165 Ah. LFP pack losted 1.073 mAh of capacity for every cycle which was more than double the loss of capacity at room temperature. Resultantly, the LFP pack would lose nearly half of its capacity after approximately 2300 cycles at high temperatures. This meant that a LFP pack in room temperature could cycle nearly 2.5 times longer than packs in high temperature situations. There was a 20% drop in the initial capacity of the LFP packs after 1000 cycles while under these simulating conditions.

Room Temperature	Capacity Fade per Cycle (mAh)	Coefficient of Determination (R^2)	High Temperature	Capacity Fade per Cycle (mAh)	Coefficient of Determination (R^2)
Charge Capacity	0.412	0.99	Charge Capacity	1.073	0.98
Discharge Capacity	0.412	0.99	Discharge Capacity	1.073	0.98

Table 1: Capacity Fade of Charge Depletion Mode from Regression Analysis

These results conveyed that it would not be ideal to run a LFP pack at high temperatures and still be able to maintaining cycling capability of LFP cells. The original capacity of LFP running the charge sustaining mode at room temperature was 4.962 Ah while the capacity after 49 cycles was 4.905 Ah. Charge sustaining mode at room temperature had twice the amount of capacity fade compared to the charge depletion mode on LFP packs. It also needed to be taken into consideration that the charge sustaining mode ran for 20% less cycles than the charge depletion mode. This revealed LFP EC cells degraded faster with a balanced distribution of charge and discharge per cycle than a predominately heavy discharge cycle at room temperature.

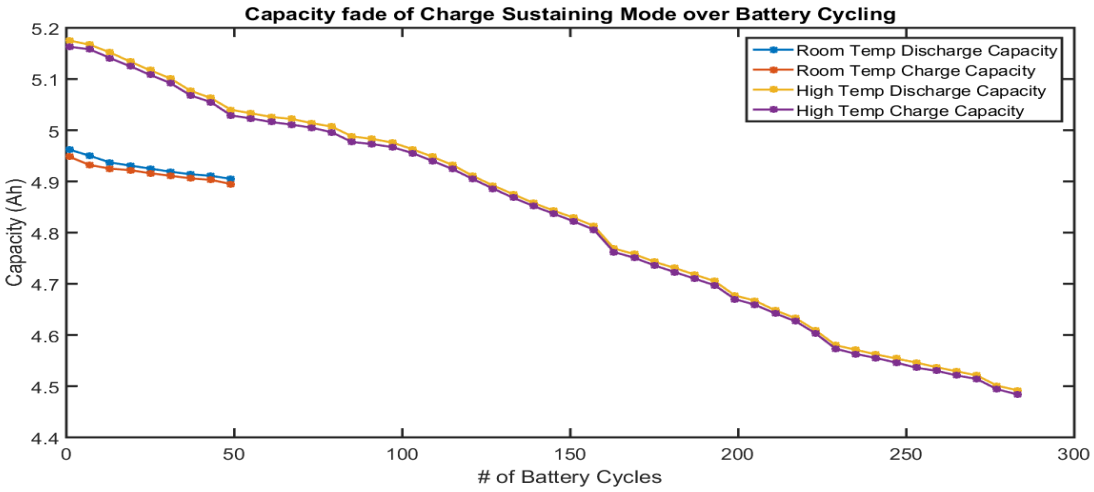

Figure 9: Capacity Fade of Charge Sustaining Mode at Room Temperature and 50C°

Results also displayed the charge sustaining mode diminished capacity almost 2.5 times quicker with 3.5 times less cycles than the charge depletion mode at 50 C°. The trend of charge sustaining mode having a larger acceleration of capacity fade in contrast to the charge depletion mode held for high temperature. These trends were alarming to the health of LFP cell capacity cycling effectiveness and it appears cycling would be heavily dependent on the C-rates as well as temperature. It appeared that LFP cells perform better when they are mainly discharged in contrast to a blend of charging and discharging at any temperature for capacity and power fade. Temperature worsened the effect of capacity fade for either case and nearly doubles the decay rate of the LIB packs.

Room Temperature	Capacity Fade per Cycle (mAh)	Coefficient of Determination (R^2)	High Temperature	Capacity Fade per Cycle (mAh)	Coefficient of Determination (R^2)
Charge Capacity	1.119	0.95	Charge Capacity	2.53	0.99
Discharge Capacity	0.967	0.96	Discharge Capacity	2.51	0.99

Table 2: Capacity Fade of Charge Sustaining Mode from Regression Analysis

The accuracy of the linear regression used to obtain capacity fade over cycling was decided with the coefficient of determination. Charge and discharge capacity fade almost mirrored each other in value for every case, so capacity of LFP cells rather than a specific charge or discharge capacity was mentioned. Accuracy of room and high temperature capacity almost completely matched the raw data values with a closeness of 98% for both charge sustaining and depletion modes. Similar to the LFP impedance analysis, results were based off of the raw data and linear regression analysis.

5.3 Modified EEM Results for LFP pack

A modified EEM as discussed above was adopted for finding the model of each cycle impedance data that was collected, an attempt at discovering possible chemical reaction trends, and a model that could predict future impedance curves over cycling. The coefficient of determination was chosen over adjusted coefficient of determination as the means to prove accuracy because frequency was the only predictor for imaginary values and cycle value for real values. Theoretical electrical values were calculated initially and optimized for improved accuracy to better match raw data. Each cycle's real and imaginary impedance data was tested with its own coefficient of determination. This process occurred due to the fact that imaginary values were dependent on frequency and real values were dependent on cycle period.

$$R^2 = 1 - \frac{\text{Residual Sum of Squares}}{\text{Total Sum of Squares}} = 1 - \frac{\sum (\text{Raw Data-EEM Data})^2}{\sum (\text{Raw Data-Mean of Raw Data})^2}$$

R^2 \ Cycle	1	213	309	345	419	465	863	881
Real |Z|	0.96	0.93	0.88	0.96	0.99	0.95	0.85	0.96
Imag |Z|	0.96	0.99	0.98	0.99	0.99	0.99	0.98	0.99

Table 3: Coefficient of Determination for Real and Imaginary |Z| Values from EEM

As seen in the tables above and below, both the real and imaginary values had high accuracy with both having at least an average accuracy higher than 93% and a minimum accuracy of 85%. These results proved that the modified EEM would be more than capable to model and predict the future trends of impedance curves over cycling time. Afterwards, optimized electrical values were tested for major and minor outliers to

improve accuracy of the trend model. The remaining electrical values were subjected to regression analysis to find an equation for each component to be placed into the final trend equation of the battery. These equations could be used to identify EC trends during the lifetime of the LFP pack.

R^2	Average Accuracy	Minimum Accuracy
Real |Z|	0.93	0.85
Imag |Z|	0.99	0.96

Table 4: Average Accuracy and Minimum Accuracy for Optimized EEM Values

Results revealed that the final transfer function produced from the Laplace transform of the total impedance of the modified EEM and the regression analysis equations of the electrical components were inadequate. Although previous results demonstrated that the modified EEM model and the transfer function created from the circuit created high accuracy results. Loss in precision occurred because regression equations for the electrical components were unsatisfactory. A maximum coefficient of determination of any chemical reaction equation was 75% which would clearly be inappropriate to pass as a good modeling result. The average accuracy of real impedance was -3300% and 32% for imaginary impedance.

Cycle	R^2 for Real |Z| before Outlier Analysis	R^2 for Img |Z| before Outlier Analysis	R^2 for Real |Z| after Outlier Analysis	R^2 for Img |Z| after Outlier Analysis
1	0.41	-2.42	0.41	Outlier
213	0.07	0.97	0.07	0.97
309	-0.19	0.927	-0.19	0.93
345	-0.26	0.89	-0.26	0.89
419	0.17	0.97	0.17	0.97
465	0.44	0.79	0.44	0.79
863	-267.03	-0.57	Outlier	-0.57
881	0.73	0.98	0.73	0.98
Average	-33.21	0.32	0.19	0.71
Percent Error due to Outliers			100.54%	123.21%

Table 5: R^2 of Final EEM Transfer Function Before and After Outlier Analysis

Obviously the coefficient of determination data appeared to have major outliers in the results or the final transfer function was grossly inadequate. Major and minor outlier analysis was done on the coefficient of determination data and resulted improved accuracy. The accuracy of real impedance improved to 20% and imaginary impedance improved to 71%. It was the conclusion that the final transfer function equation produced would be insufficient to be used to model LFP pack impedance curves over cycling. Additionally, the electrical component equations created would not be a good choice in finding trends of the chemical reactions for LFP cells.

This loss in certainty for chemical reaction regression equations and the final transfer function happened because not enough periodic cycle impedance data was assembled. If more data was accumulated during the experiment, there would most likely have been a dramatic improvement in the accuracy of the chemical and transfer function equations.

It would have been favorable to collect more data, but the Parstat 2273 malfunctioned three times during the experiment which created gaps in the data gathering. The concluding remarks to the modified EEM would be that it could be adopted for future experiments, but careful data collection would be required.

5.4 Effects of LFP Performance on Charge Depletion Mode HEVs

One study predicted that the average lifetime of a vehicle had been trending from 12.5 years to 16.9 year from the years of 1980-1990 [57]. If this trend held true than the average life of a vehicle would be around 20 years in the year 2010. To simplify this matter, it was stated that the lifetime of a vehicle was ten years and the vehicle drove 12,000 miles a year to have a lifetime of 120,000 miles. Otherwise the lifetime of the vehicle would be in the range of 240,000 miles which seemed to be unrealistic. The lifetime of a vehicle was brought up to illustrate the fact that HEVs using electric only drive modes would not last even a year under hot and arid conditions.

LFP pack under charge depletion mode drove under an electric only drive for approximately 5300 miles. This understanding was based off that every five cycles carried out were the charge depletion mode current profile followed by constant charge and discharge cycles. The LIB pack could be concluded to have run 715 cycles under only the current profile and the current profile represented a distance of 7.45 miles. Generally, the life of an AB pack would be around 70-100% capacity range and the capacity to obtain 70% for LFP under high temperature and charge depletion mode would

be 1460 cycles. This would mean that an HEV using an electric only drive mode would be able to drive for 10,600 miles under high temperatures.

This lifetime for a HEV would be seen as an unacceptable situation for the average consumer and they would be less likely to buy an HEV if this knowledge was prevalent. The torque and power performance of the HEV would also be reduced to half after less than a year's use of electric only drive mode. These results would only hold true if HEVs only drove during high temperatures and drove under electric only mode. Most places in the world would have extreme temperatures for 3-4 months out of the year.

If the vehicle was only driven during those times, the battery pack duration would improve by a factor of two and three respective of a reduction in power and energy fade. HEVs generally ran under a charge depletion mode for relatively 30% of the time [58,59]. If that was taken into consideration with previous assumptions, then the life of the battery would increase by 6-10 times. Overall, HEVs would last 2-3 times longer if driving with an electric only mode and 6-10 times longer with varied driving modes.

5.5 Crystallization trends for LFP

SEM images were produced from LFP cells at a preliminary state, and after the LFP packs ran the current profiles of charge sustaining and depleting modes of EVs. The results of the fresh LFP cell's image at 50μm and 10μm showed a mixture of small and large irregular particle sizes that were unequally distributed throughout the sample. There was a glossy white coating on a majority of the crystalline structures which could

indicate the carbon coating on the LFP. As seen from the figure, this coating of carbon was uneven and could be a result of the synthesis process of LFP cells. When the image was zoomed to 10μm, the unorganized placement of crystalline particles was maintained for the sample.

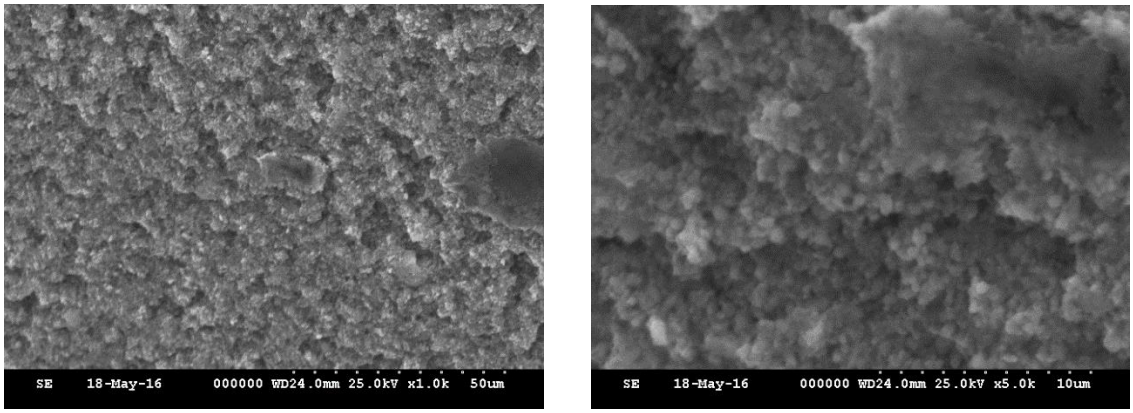

Figure 10: Images of Fresh LFP, 50μm (left) and 10μm (right)

A dramatic increase of crystalline growth could be seen on LFP cells after running 1007 cycles under the charge depletion mode. The same uniformity of particle distribution seen from the fresh LFP cells was preserved for the cycled LFPs. It was interesting to note that there was a decrease in the glossy white coating of carbon. This could be a sign of the degradation of the carbon coating on LFP particles. Also, a majority of the sample had only small LFP particles compared to the combination of small and large particles seen in the fresh sample.

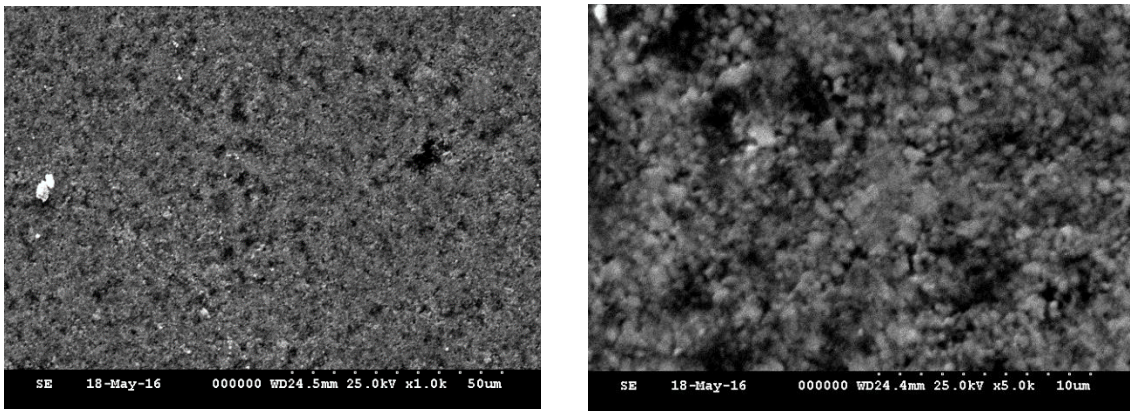

Figure 11: Images of Charge Depletion After Cycling, 50μm (left) and 10μm (right)

Samples of new LFP and the charge depleted LFP after being cycled were tested using XRD. The settings for XRD was to test the samples under room temperature conditions, have a scanning range of 20-80°, a power setting of 40kV, and a produce a wavelength of 1.54 Å from anodic copper material. Samples were indexed under the olivine structure of $LiFePO_4$ to correlate if there were similar compositions. XRD analysis showed signs of a slight phase change on the crystal structure of the charge depleted material while no phase change was seen for the fresh sample. The phase change on the charge depleted sample appeared to be a uniform strain on the material with a few irregular conjoined peaks which could represent non-uniformed micro-strains.

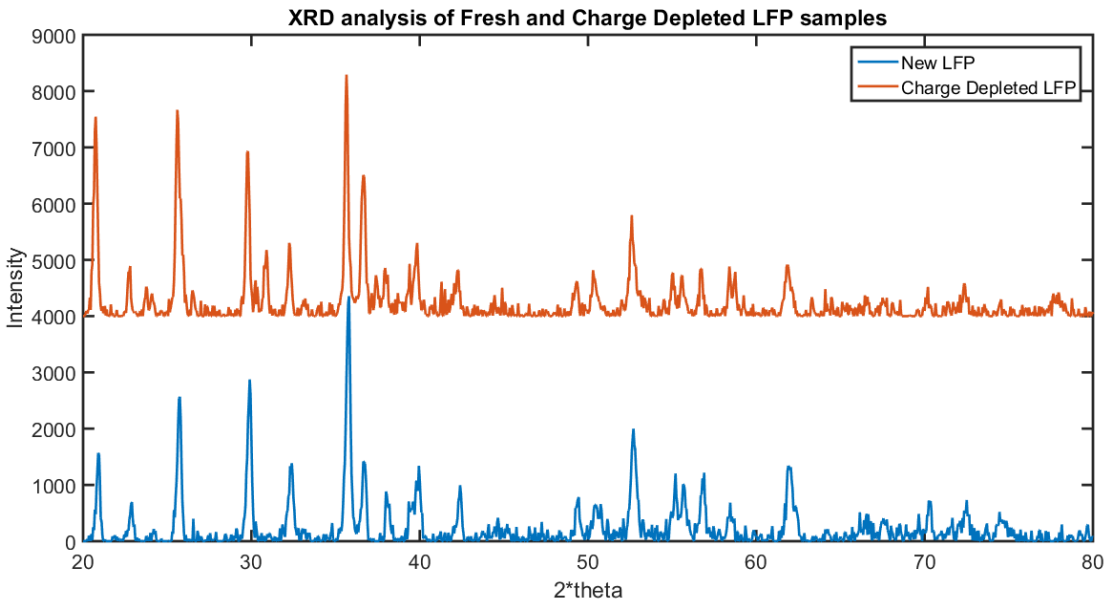

Figure 12: XRD Results of Fresh and Charge Depleted LFP Samples

These possible micro-strains could indicate there were small amounts of impurities in the LFP battery material. Average d-spacing, FWHM, and crystal size of new LFP in contrast with charge depleted LFP revealed a slight decrease in crystal size while an increase in d-spacing, and FWHM. The increase in d-spacing confirmed a local lattice distortion, and micro-strains from the peak broadening of the FWHM. A slight decrease in crystal size could represent a slow degradation of the chemical reaction quality.

	Fresh					Charge Depleted			
2*Θ	Intensity	d_{hkl} (Å)	FWHM (mRads)	Size (nm)	2*Θ	Intensity	d_{hkl} (Å)	FWHM (mRads)	Size (nm)
20.9	1569	2.16	3.49	42.55	20.75	3545	2.17	5.24	28.32
25.75	2567	1.77	4.36	35.28	25.6	3667	1.78	6.98	22.02
29.9	2876	1.54	5.24	30.55	29.75	2916	1.55	4.36	36.60
35.8	4356	1.32	5.24	32.65	35.65	4292	1.32	3.49	48.89
36.65	1420	1.29	6.11	33.01	36.70	2476	1.29	5.24	33.03
52.7	2000	0.97	6.11	37.46	52.60	1797	0.97	6.11	37.37
Average		1.51	4.95	35.25	Average		1.52	5.24	34.37

Table 6: XRD Analysis Results for Fresh and Charge Depleted LFP Samples

6 CONCLUSION

Results of the experiment revealed that LFP packs running a charge depletion mode current profile had a small capacity fade. At higher temperatures, the capacity fade nearly doubled and the power fade of LFP cells would see a dramatic drop in power every 900 cycles. These results meant LFP packs running a charge depletion mode at high temperature would be inoperable for HEV applications after 900 cycles for power applications and 1450 cycles for energy applications. This would mean HEVs driving under electric only mode during hot conditions could drive 10,500 miles before having to replace the battery. It would take half the time for HEVs to lose power operations such as towing under the same settings.

A new high fidelity EEM was established by modifying a Randles circuit with a BVD circuit and a newly invented electrical and modeling component called the ICPE. The

results of the modified EEM illustrated that the model and the transfer function could accomplish high accuracy. This high accuracy could only be obtained if data was careful gathered during the experiment. Otherwise, the overall accuracy of the model to predict chemical reactions and impedance cycle trends would be diminished. SEM images of LFP cells before cycling indicated a mixture of small and large crystalline parts that were unevenly coated with carbon.

After LFP cells were cycled under a charge depletion mode, a large amount of growth and a reduction in carbon coating occurred on the particles. The size of the particles reduced from the charge depletion cycling, but the unorganized uniformity found in the fresh LFP sample were maintained in the cycled LFP sample. XRD results expressed that there was a minor uniformed strain throughout LFP sample after cycling under a charge depleting profile. There were also slight impurities in the material seen as non-uniformed micro-strains and a marginal decrease in crystal size.

7 FUTURE WORK

Possible work to create an understanding on the effects on performance of EVs would be to invent and optimize a drive cycle. The new drive cycle could incorporate pre-existing drive cycles which would simulate human driving patterns. This new drive cycle as well old drive cycles could simulate driving conditions in multiple types of weather circumstances. It would have a spectrum of cold to hot temperatures as well as dry to moist settings.

To optimize these experiments further, a changing environment could be simulated instead of a constant temperature analysis. These experiments should check chemical reactions with XRD, EIS, cyclic voltammetry, energy-dispersive x-ray spectroscopy, and other methods. Lastly, the analysis of ABs being used in a secondary application should be investigated for optimal battery use and economic benefits.

7.1 AZ-01 Drive Cycle

Many different types of drive cycles were originally created to test the emissions and fuel economy of vehicles in the United States [33]. The list of drive cycles could be broken up into categories and subcategories which most EVs were tested under light-duty vehicles [32]. Drive cycles under these categories were converted from a velocity profile that a dynamometer captured into a current profile the vehicle would demand from the battery of an EV [34]. Generally, the drive cycles that were used are the US06 Supplemental FTP, the UDDS [35], SC03 Supplemental FTP, and the HWFET. These driving schedules simulate aggressive, city, air conditioning loading, and highway driving of vehicles.

Most research in the field of EVs was being done to test an individual drive cycle to a battery pack system rather than designing a modified drive cycle from the pre-existing cycles [46,60,61]. Possible research could be done by combining the SC03, UDDS, US06, and HWFET to better describe driving conditions in Arizona. The new drive called the AZ-01 would begin with half of the SC03 cycle to mimic Arizona drivers cooling down their vehicle from high temperature to low temperature.

Next, the transient phase of the UDDS would be added to imitate normal city driving followed by the first quarter and last quarter of the HWFET to represent the average person driving to or from work on the freeway. The last section of the AZ-01 would incorporate sections of the US06 to match a person aggressive driving to make the last distance to work or to get home.

7.2 Arizona Yearly Temperature Effects

This new drive schedule would more accurately display driving conditions in Arizona and the AZ-01 could test batteries under hot and arid conditions to replicate Arizona summers. To get a better understanding of how a battery pack would fade would be to run the AZ-01 drive schedule at a constant temperature as well as different temperatures [62]. The mixture of temperatures could resemble the temperature change in Arizona by having an incremental scaling of temperature. This scale would go from cool temperatures to warm temperatures for three-fourths of the battery pack's life symbolizing the relatively cool weather for most of the year. Then the pack would be running under hot and arid conditions for the last quarter of its life to suggest summer heats.

7.3 Chemical and Physical Properties of Proposed Experiments

The possible experiments above could be analyzed throughout their duration for their chemical electrical properties. Analysis techniques that would be done are energy-dispersive x-ray spectroscopy, x-ray photoelectron spectroscopy, XRD, EIS, and cyclic

voltammetry [63]. These methods would allow the collection of the amount, size of crystalline structure, and type of element inside the bulk of the material as well as the surface. Also, they would show the impedance, reduction and oxidation process happening in an EC. These techniques such as energy-dispersive x-ray spectroscopy would be important in showing the efficiency of the chemical reaction happening by observing the amount of elements in the bulk of EC.

X-ray photoelectron spectroscopy could show surface contaminants of foreign elements observed from the manufacturing process or the degradation of the material during battery cycling which could lead to an increase in impedance. XRD could create a comparison with the size of crystalline elements layers on the surface and in the bulk of the material with the values of impedance over time to find relationships [64]. These relationships could correlate certain chemical reactions having a greater effect on the impedance and capacity of the EC using EIS in conjunction with the other methods. Resultantly, it would show how to prevent energy and power loss during the lifetime of the battery by understanding which chemical reactions produce the effect. Some other variables that could be monitored are conductivity, reversibility, and stability using cyclic voltammetry on the EC [65].

7.4 Second Life of Automotive Batteries

Second life batteries were batteries that served as fresh batteries to store energy in a specific system, but could no longer maintain the required expectations of the system. In this case, second life batteries would be collected from EVs.

The market for second life batteries would most likely grow proportionally with the EV market due to the fact that retired ABs could be gathered to supply second life needs. It would be economically vital that second life batteries are harnessed for utility support, off-grid energy, discount savings for consumers, and other tertiary systems.

These applications as well as many other opportunities show there could be a big potential for second life batteries, but utility companies need to seize this situation to be frontrunners. One huge economic benefit would be storing the wasted excess electricity during low demand times and supplying it during peak hours. The electric infrastructure has been well established and there would only be a marginal cost to install a second life storage system at residential areas. Utility companies could negotiate prices to rent the storage capability of EVs batteries based on the modified EEM which shows the trend of energy and power fade over the vehicle lifetime.

REFERENCES

[1] Ajanovic A, The future of electric vehicles: prospect and impediments, WIREs Energy and Environment, 4 (2015) 521-536.

[2] Schaeck S, Karspeck T, Ott C, Weckler M, Stoermer A.O, A field operational test on valve-regulated lead-acid absorbent-glass-mat batteries in micro-hybrid electric vehicles. Part I. Results based on kernel density estimation, J. Power Sources, 196 (2011) 2924-2932.

[3] Jung D.B, Cho S.W, Park S.J, Min K.D, Application of a modified thermostatic control Strategy to parallel mild HEV for improving fuel economy in urban driving conditions, J. Int. Automotive Technology, 17 (2016) 339-346.

[4] Aghaei J, Nezhad A.E, Rabiee A, Rahimi Ehsan, Contribution of Plug-in Hybrid Electric Vehicles in power system uncertainty management, Renewable and Sustainable Energy Reviews, 59 (2016) 450-458.

[5] Johnson D.A, Reid M.A, Chemical and Electrochemical Behavior of the Cr(III)/Cr(II) Half-Cell in the Iron-Chromium Redox Energy Storage System, J. Electrochemical Society, 132 (1985) 1058-1062.

[6] Powers R.A, Advances and Trends in Primary and Small Secondary Batteries, IEEE AES Systems Magazine, 9 (1994) 32-36.

[7] Rogulski Z, Czerwinski A, Cathode Modification in the Leclanché cell, J. Solid State Electrochem, 7 (2003) 118-121.

[8] Friedman M, McCauley C.E, The Ruben Cell-A New Alkaline Primary Dry Cell Battery, Transactions of the Electrochemical Society, 92 (1947) 195-215.

[9] Budde-Meiwes H, Drillkens J, Lunz B, Muennix J, Rothgang S, Kowal J, Sauer DU, A review of current automotive battery technology and future prospects, J. Automobile Engineering, 227 (2013) 761–776.

[10] Dubaniewicz Jr. TH, DuCarme JP, Further study of the intrinsic safety of internally shorted lithium and lithium-ion cells within methane-air, J. Loss Prevention in the Process Industries, 32 (2014) 165–173.

[11] Dubaniewicz Jr. TH, DuCarme JP, Are lithium ion cells intrinsically safe?, IEEE Transactions on Industry Applications, 49 (2013) 2451–2460.

[12] Zaghib K, Dubé J, Dallaire A, Galoustov K, Guerfi A, Ramanathan M, Benmayza A, Prakash J, Mauger A, Julien CM, Enhanced thermal safety and high power performance of carbon coated $LiFePO_4$ olivine cathode for Li-ion batteries, J. Power Sources, 219 (2012) 36–44.

[13] Xu J, Liu B, Wang L, Shang S, Dynamic mechanical integrity of cylindrical lithium-ion battery cell upon crushing, J. Engineering Failure Analysis, 53 (2015) 97-110.

[14] Larsson F, Andersson P, Blomqvist P, Loren A, Mellander B.E, Characteristics of lithium-ion batteries during fire tests, J. Power Sources, 271 (2014) 414-420.

[15] Y. Zhang, C.Y. Wang, X. Tang, Cycling degradation of an automotive $LiFePO_4$ lithium-ion battery, J. Power Sources, 196 (2011) 1513-1520.

[16] C. Capasso, O. Veneri, Experimental analysis on the performance of lithium based batteries for road full electric and hybrid vehicles, J. Applied Energy, 136 (2014) 921-930.

[17] J. Groot, M. Swierczynski, A.I. Stan, S.K. Kær, On the complex ageing characteristics of high-power $LiFePO_4$/graphite battery cells cycled with high charge and discharge currents, J. Power Sources 286 (2015) 475-487.

[18] M. Swierczynski, D.I. Stroe, A.I Stan, R. Teodorescu, S.K Kær, Lifetime estimation of the nanophosphate $LiFePO_4$/C battery chemistry used in fully electric vehicles, IEEE Transactions on Industry Applications 51 (2015) 3453-3461.

[19] Samadani E, Farhad S, Scott W, Mastali M, Gimenez L, Fowler M, Fraser R.A, Empirical Modeling of Lithium-ion Batteries Based on Electrochemical Impedance Spectroscopy Tests, J. Electrochimica Acta, 160 (2015) 169-177.

[20] J. Li, M.S Mazzola, Accurate battery pack modeling for automotive applications, J. Power Sources, 237 (2013) 215-228.

[21] Sung W, Shin C.B, Electrochemical model of a lithium-ion battery implemented into an Automotive battery management system, J. Computers and Chemical Engineering, 76 (2015) 87-97.

[22] Li S.E, Wang B, Peng H, Hu X, An electrochemistry-based impedance model for lithium-ion batteries, J. Power Sources, 258 (2014) 9-18.

[23] He H, Zhang Y, Xiong R, Wang C, A novel Gaussian model based battery state estimation Approach, J. Applied Energy, 151 (2015) 41-48.

[24] Azar A.T, Fast neural network learning algorithms for medical applications, Neural Comput & Applic, 23 (2013) 1019-1034.

[25] Nikonenko V.V, Kozmai A.E, Electrical equivalent circuit of an ion-exchange Membrane system, J. Electrochimica Acta, 56 (2011) 1262-1269.

[26] Wang B, Li S.E, Peng H.P, Liu Z, Fractional-order modeling and parameter Identification for lithium-ion batteries, J. Power Sources, 293 (2015) 151-161.

[27] Alavi S.M.M, Birkl C.R, Howey, Time-domain fitting of battery electrochemical impedance models, J. Power Sources 288 (2015) 345-352.

[28] Zou Y, Li S.E, Shao B, Wang B, State-space model with non-integer order derivatives for lithium-ion battery, J. Applied Energy, 161 (2016) 330-336.

[29] Pattipati B, Sankavaram C, Pattipati K.R, System Identification and Estimation Framework for Pivotal Automotive Battery Management System Characteristics, IEEE Transactions on Systems, 41 (2011) 869-884.

[30] Wu G, Zhang X, Dong Z, Powertrain architectures of electrified vehicles: Review, Classification and comparison, J. Franklin Institute, 352 (2015) 425-448.

[31] Hutchinson T, Burgess S, Herrmann G, Current hybrid-electric powertrain architectures: Applying empirical design data to life cycle assessment and whole-life cost analysis, J. Applied Energy, 119 (2014) 314-329.

[32] Cited on April 4th, 2016, https://www3.epa.gov/.

[33] Cited on April 4th, 2016, https://www.fueleconomy.gov/feg/how_tested.shtml

[34] Peterson S, Apt J, Whitacre J.F, Lithium-ion battery cell degradation resulting from Realistic vehicle and vehicle-to-grid utilization, J. Power Sources, 195 (2010) 2385-2392.

[35] Kruse R, Huls T, Development of the Federal Urban Driving Schedule, SAE Technical Paper, 730553 (1973).

[36] Chew K.W, Koay C.K, Yong Y.R, ADVISOR Simulation of Electric Vehicle Performance On Various Driving Cycles, Int. J. Innovative Science, Engineering & Technology, 1 (2014) 70-76.

[37] Mayyas A.R, Prucka R, Haque I, Pisu P, Model-based automotive system integration: using vehicle hardware in-the-loop simulation for an integration of advanced hybrid electric powertrain, Int J. Electric and Hybrid Vehicles, 5 (2013) 215-232.

[38] Han J, Jia Y, Jin S, Jing Y, Tillard M, Belin C, Morphology and electrochemistry of spinel Li-Mn-O optimized by composite technology, Energy, 31 (2006) 2088-2093.

[39] Chen Y.C, Chen J.M, Huang Y.H, Lee Y.R, Shih H.C, Size effect of tin oxide Nanoparticles on high capacity lithium battery anode materials, Surface & Coatings Technology, 202 (2007) 1313-1318.

[40] Huang J, Ge H, Li Z, Zhang J, Dynamic Electrochemical Impedance Spectroscopy of a Three-Electrode Lithium-Ion Battery during Pulse Charge and Discharge, J. Electrochimica Acta, 176 (2015) 311-320.

[41] Farmann A, Waag W, Sauer D.U, Adaptive approach for on-board impedance parameters and voltage estimation of lithium-ion batteries in electric vehicles. J. Power Sources, 299 (2015) 176-188.

[42] Hirschorn B, Orazem M, Tribollet B, Vivier V, Frateur I, Musiani M, Constant-Phase-Element Behavior Caused by Resistivity Distributions in Films, J. Electrochemical Society, 157 (2010) C452-C457.

[43] Dhirde A.M, Dale N.V, Salehfar H, Mann M.D, Han T.H, Equivalent Electric Circuit Modeling and Performance Analysis of a PEM Fuel Cell Stack Using Impedance Spectroscopy, IEEE Transactions on Energy Conversion, 25 (2010) 778-786.

[44] Wang B, Li S.E, Peng H, Liu Z, Fractional-order modeling and parameter identification for lithium-ion batteries, J. Power Sources, 293 (2015) 151-161.

[45] Liu Y, Liu Q, Li Z, Ren Y, Xie J, He H, Xu F, Failure Study of Commercial $LiFePO_4$ in over-Discharge Conditions Using Electrochemical Impedance Spectroscopy. J. Electrochemical Society, 161 (2014) A620-A632.

[46] Duong V.H, Bastawrous H.A, Lim K, See K.W, Zhang P, Dou S.X, Online state of charge and model parameters estimation of the $LiFePO_4$ battery in electric vehicles using multiple adaptive forgetting factors recursive least-squares, J. Power Sources, 296 (2015) 215-224.

[47] Loveday D, Peterson P, Rodgers B, Evaluation of organic coatings with electrochemical impedance spectroscopy – Part 1: fundamentals of Electrochemical impedance spectroscopy, JCT Coatings Tech, 1 (2004) 46-52.

[48] Roberts M.R, Madsen A, Nicklin C, Rawle J, Palmer M.G, Owen J.R, Hector A.L, Direct Observation of Active Material Concentration Gradients and Crystallinity Breakdown in $LiFePO_4$ Electrodes During Charge/Discharge Cycling of Lithium Batteries, J. Physical Chemistry, 118 (2014) 6548-6557.

[49] KIM S, KIM U, KIM J, CHO W, Synthesis of porous $LiFePO_4$ cathode material by citrate process for lithium ion battery, J. Ceramic Society of Japan, 124 (2016) 145-149.

[50] Macia N.F, Thaler G.J, Modeling & Control of Dynamic Systems, Thomson Delmar Learning, 2005.

[51] Jin H, Dong S.R, Luo J.K, Milne W.I, Generalised Butterworth-Van Dyke Equivalent Circuit for thin-film bulk acoustic resonator, Electronics Letters, 47 (2011) 1-2.

[52] Meftah R, Meyer Y, Equivalent-Circuit Model for Quartz Resonators Effects of Finite Element Analysis, Acceleration, and Mass Loading, Mechanics of Advanced Materials and Structures, 20 (2013) 774-790.

[53] Mareschal O, Loiseau S, Fougerat A, Valbin L, Lissorgues G, Saez S, Dolabdjian C, Bouregba R, Poullain G, Piezoelectric Aluminum Nitride Resonator for Oscillator, IEE Transactions on Ultrasonics, Ferroelectrics, and Frequency Control, 56 (2010) 513-517.

[54] Ding J, Su Z, Zhang Y, Two-step synthesis of nanocomposite $LiFePO_4$/C cathode Materials for lithium ion batteries, New J. Chem, 40 (2016) 1742-1746.

[55] Gorzkowska I, Jozwiak P, Garbarczyk J.E, Wasiucionek M, Julien C.M, Studies on Glass Transition of Lithium-Iron Phosphate Glasses, J. Thermal Analysis and Calorimetry, 93 (2008) 759-762.

[56] Dompablo M.E.A, Gallardo-Amores J.M, Amador U, Lithium Insertion in the High-Pressure Polymorph of $FePO_4$ Computational Predictions and Experimental Findings, Electrochemical and Solid-State Letters 8 (2005) A564-A569.

[57] Kim H.C, Keoleian G.A, Grande D.E, Bean J.C, Life Cycle Optimization of Automobile Replacement: Model and Application, J. Environ Sci. Technol., 37 (2003) 5407-5413.

[58] Gong Q, Li Y, Peng Z.R, Trip-Based Optimal Power Management of Plug-in Hybrid Electric Vehicles, IEEE Transactions Vehicular Technology, 57 (2008) 3393-3401.

[59] Wirasingha S.G, Emadi A, Classification and Review of Control Strategies for Plug-In Hybrid Electric Vehicles, IEE Transcations Vehicular Technology, 60 (2011) 111-122.

[60] Yang F, Xing Y, Wang D, Tsui K.L, A comparative study of three model-based Algorithms for estimating state-of-charge of lithium-ion batteries under a new combined dynamic loading profile, J. Applied Energy, 164 (2016) 387-399.

[61] Suri G, Onori S, A control-oriented cycle-life model for hybrid electric vehicle lithium-ion batteries, J. Energy, 96 (2016) 644-653.

[62] Samadani E, Mastali M, Farhad S, Fraser R.A, Fowler M, Li-ion battery performance and degradation in electric vehicles under different usage scenarios, Int J. Energy research, 40 (2016) 379-392.

[63] Venckute V, Miskinis J, Kazlauskiene V, Salkus T, Dindue A, Kanepe Z, Ronis J, Maneikis A, Lelis M, Kezionis A, Orliukas A.F, XRD, XPS, SEM/EDX and Broadband Impedance spectroscopy study of pyrophosphate (LiFeP2O7 and Li0.9Ti0.1P2O7) ceramics, J. Phase transitions, 87 (2014) 438-451.

[64] Shu H, Chen M, Wen F, Fu Y, Liang Q, Yang X, Shen Y, Liu L, Wang X, Fast Li-Ion conductive La0.56Li0.33TiO3 inlaid LiFePO4/C microspheres with enhanced high-rate performance as cathode materials, J. Electrochimica Acta, 152 (2015) 368-377.

[65] Li X, Zhang X, Zhang Z, Synthesis of high-performance LiFePO4/C composite with a grape bunch structure through the hydrothermal method, J. Ionics, 20 (2014) 1275-1283.

APPENDIX A

FUNDAMENTAL ELECTRICAL ELEMENT EQUATIONS

All Laplace transforms calculated assumed initial conditions of zero to reduce complexity of transformations.

Laplace transform of a resistor:

Fundamental equation of a resistor

$$V = I*R$$

Laplace transform of fundamental equation

$$\mathcal{L}\{v(t)\} = \mathcal{L}\{I(t)\}*\mathcal{L}\{R(t)\} \rightarrow$$

$$V(s) = I(s)*R(s) \rightarrow \frac{V(s)}{I(s)} = R(s) \rightarrow Z(s) = R$$

Laplace transform of a capacitor:

Fundamental equation of a capacitor

$$i = C*\frac{dv}{dt} \rightarrow v = \frac{1}{C}\int i*dt$$

Laplace transform of fundamental equation

$$\mathcal{L}\{v(t)\} = \mathcal{L}\{\frac{1}{C}\int i*dt\} \rightarrow$$

$$\mathcal{L}\{V(s)\} = \frac{I(s)}{s*C} \rightarrow \frac{V(s)}{I(s)} = \frac{1}{s*C} \rightarrow Z(s) = \frac{1}{s*C}$$

Laplace transform of an inductor:

Fundamental equation of an inductor

$$v = L*\frac{di}{dt}$$

Laplace transform of fundamental equation

$$\mathcal{L}\{v(t)\} = \mathcal{L}\{L*\frac{di}{dt}\} \rightarrow$$

$$V(s) = s*L*I(s) \rightarrow \frac{V(s)}{I(s)} = s*L \rightarrow Z(s) = s*L$$

Fundamental equation of CPE:

$$Z(s) = \frac{1}{Q_1*s^{n_1}} \qquad C \approx Q_1 \qquad 0 < n_1 < 1$$

Fundamental equation of ICPE:

$$Z(s) = \frac{1}{Q_2 * s^{n_2}} \rightarrow Z(s) = \frac{s^{n_2}}{Q_2} = L * s^{n_2} \qquad L \approx \frac{1}{Q_2} \qquad 0 < n_2 < 2$$

List of impedance symbols and electrical equations for chemical reactions:

Ohmic Resistance

$$Z_{Ohmic} = R_{ohmic}$$

Charge Transfer Resistance

$$Z_{CTresist} = R_{CT}$$

Coating Capacitance

$$Z_{Coating} = \frac{1}{s * C_{oat}}$$

Double Layer Capacitance

$$Z_{DoubleLayer} = \frac{1}{Q_1 * s^{n_1}}$$

Charge Transfer Inductance

$$Z_{CTinduct} = L * s$$

Current Collector Degradation and Test Equipment Inductance

$$Z_{ICPE} = \frac{s^n}{Q_2} = L * s^{n_2}$$

APPENDIX B

IMPEDANCE TRANSFER FUNCTION CALCULATIONS

Total Impedance of Modified EEM:

$$Z_{Total} = Z_{Ohmic} + Z_{ICPE} + [(Z_{CTresist} + Z_{CTinduct} + Z_{DoubleLayer}) || Z_{Coating}]$$

$$= Z_{Ohmic} + Z_{ICPE} + \frac{(Z_{CTresist} + Z_{CTinduct} + Z_{DoubleLayer}) * Z_{Coating}}{Z_{CTresist} + Z_{CTinduct} + Z_{DoubleLayer} + Z_{Coating}}$$

$$= R_{ohmic} + \frac{s^{n_2}}{Q_2} + \frac{\left(R_{CT} + L*s + \frac{1}{s^{n_1}*Q_1}\right) * \frac{1}{s*C_{Coat}}}{R_{CT} + L*s + \frac{1}{s^{n_1}*Q_1} + \frac{1}{s*C_{Coat}}}$$

$$= R_{ohmic} + \frac{s^{n_2}}{Q_2} + \frac{R_{CT} + L*s + \frac{1}{s^{n_1}*Q_1}}{s^2*L*C_{Coat} + s*R_{CT}*C_{Coat} + \frac{s*C_{Coat}}{s^{n_1}*Q_1} + 1}$$

$$= \frac{R_{ohmic}}{1} + \frac{s^{n_2}}{Q_2} + \frac{s^{n_1+1}*L*Q_1 + s^{n_1}*R_{CT}*Q_1 + 1}{s^{n_1+2}*L*Q_1*C_{coat} + s^{n_1+1}*R_{CT}*Q_1*C_{coat} + s*C_{coat} + s^{n_1}*Q_1}$$

$$= \left[\frac{R_{ohmic}}{1} * \left(\frac{s^{n_1+2}*L*Q_1*C_{coat} + s^{n_1+1}*R_{CT}*Q_1*C_{coat} + s*C_{coat} + s^{n_1}*Q_1}{s^{n_1+2}*L*Q_1*C_{coat} + s^{n_1+1}*R_{CT}*Q_1*C_{coat} + s*C_{coat} + s^{n_1}*Q_1}\right) * \frac{Q_2}{Q_2}\right] +$$
$$\left[\frac{s^{n_2}}{Q_2} * \left(\frac{s^{n_1+2}*L*Q_1*C_{coat} + s^{n_1+1}*R_{CT}*Q_1*C_{coat} + s*C_{coat} + s^{n_1}*Q_1}{s^{n_1+2}*L*Q_1*C_{coat} + s^{n_1+1}*R_{CT}*Q_1*C_{coat} + s*C_{coat} + s^{n_1}*Q_1}\right) * \frac{1}{1}\right] +$$
$$\left[\frac{s^{n_1+1}*L*Q_1 + s^{n_1}*R_{CT}*Q_1 + 1}{s^{n_1+2}*L*Q_1*C_{coat} + s^{n_1+1}*R_{CT}*Q_1*C_{coat} + s*C_{coat} + s^{n_1}*Q_1} * \frac{Q_2}{Q_2} * \frac{1}{1}\right]$$

Numerator of final impedance transfer function

$$s^{n_1+n_2+2}\left(L*C_{coat}*Q_1\right) + s^{n_1+n_2+1}\left(R_{CT}*C_{coat}*Q_1\right) + s^{n_1+2}\left(R_{ohmic}*L*Q_1*Q_2*C_{coat}\right) +$$
$$s^{n_1+1}\left[\left(R_{CT}*R_{ohmic}*Q_1*Q_2*C_{coat}\right) + \left(L*Q_1*Q_2\right)\right] + s^{n_2+1}\left(C_{coat}\right) + s^{n_1+n_2}\left(Q_1\right) +$$
$$s*\left(R_{ohmic}*Q_2*C_{coat}\right) + s^{n_1}\left[\left(R_{ohmic}*Q_1*Q_2\right) + \left(R_{CT}*Q_1*Q_2\right)\right]$$

Denominator of final impedance transfer function

$$s^{n_1+2}*L*Q_1*Q_2*C_{coat} + s^{n_1+1}*R_{CT}*Q_1*Q_2*C_{coat} + s*C_{coat}*Q_2 + s^{n_1}*Q_1*Q_2$$

APPENDIX C

THEORETICAL ELECTRICAL ELEMENT CALCULATIONS

Ohmic resistances were taken from the RC network graph at the point where the impedance curve crossed the x-axis. The combined ohmic and charge transfer resistances were taken at the second time the impedance curve crossed the x-axis. An example of the method on how to calculate the theoretical values for the modified EEM can be seen below.

Cycle 213:

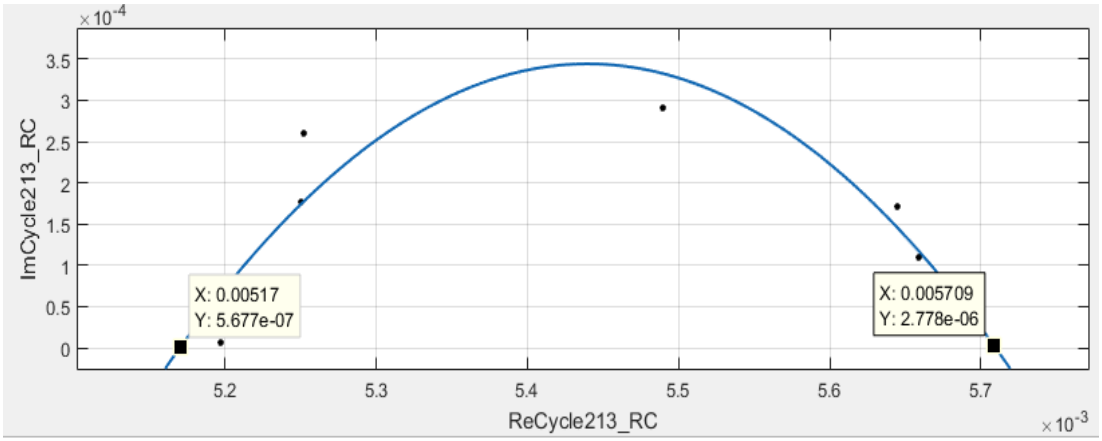

Figure 13: RC Network Section of Cycle 213 Impedance with Reference Points

Ohmic Resistance and Charge Transfer Resistance

$$R_{Ohmic}=5.17m\Omega$$

$$R_{CT} = R_{Ohmic+CT}-R_{Ohmic} = 5.71m\Omega - 5.17m\Omega = 0.54m\Omega$$

Coating Capacitance

$$\omega = \frac{1}{R_{CT}*C_{coat}} \rightarrow C_{coat} = (R_{CT}*\omega)^{-1}$$

$$C_{coat} = (\omega_{RCpeak}*R_{ct})^{-1} = (2*\pi*f_{RCpeak}*R_{ct})^{-1}$$

$$= (2*\pi*41.75Hz*0.54m\Omega)^{-1} = 7.07F$$

Double Layer Capacitance

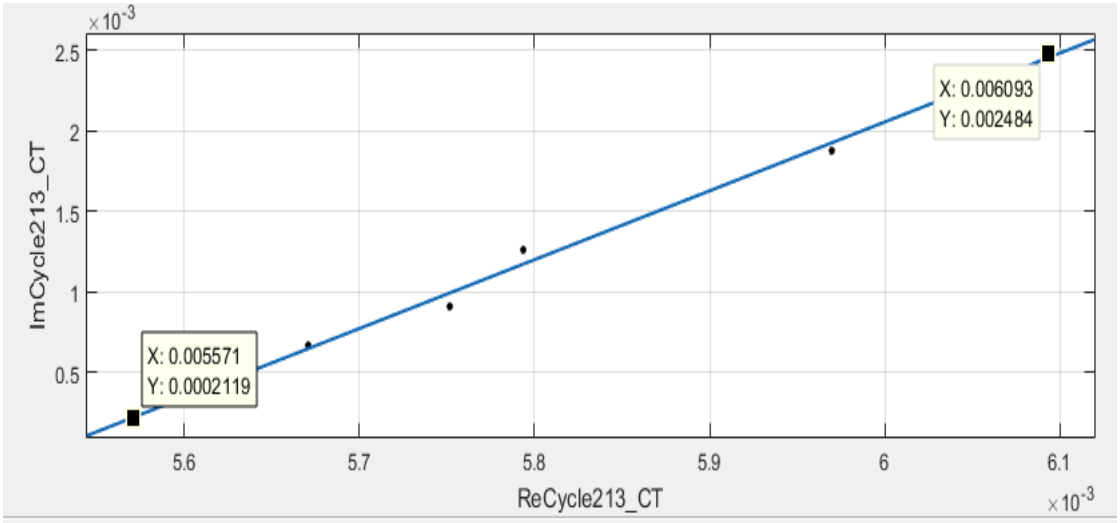

Figure 14: Capacitive Tail of Cycle 213 Impedance with Reference Points

$$|Z| = \sqrt{(R_{arbitrary})^2+(\frac{1}{\omega*Q_1})^2} \rightarrow Q_1 = \left(\sqrt{(|Z|)^2-(R_{arbitrary})^2}*\omega\right)^{-1}$$

$$|Z| = \sqrt{(X_{finalLength}-X_{InitialLength})^2+(Y_{finalLength})^2}$$

$$|Z| = \sqrt{(0.00609337-0.00557085)^2+(0.00248406)^2} = 0.002538421$$

$$Q_1 = \left(\sqrt{(0.002538421)^2-(0.00609337-0.00557085)^2}*(2*\pi*240mHz)\right)^{-1}$$

$$Q_1 = 267.52F$$

$$n_1 = \sin(|\theta|) = \sin\left[\tan^{-1}\left(\frac{Y_{finalLength}}{X_{finalLength}-X_{InitialLength}}\right)\right] = 0.98$$

Charge Transfer Inductance

$$\omega = \frac{1}{\sqrt{L*Q_1}} \rightarrow L = \frac{1}{\sqrt{Q_1*\omega^2}}$$

$$L = (267.52F*2*\pi*12.69Hz)^{-1} = 0.59\mu H$$

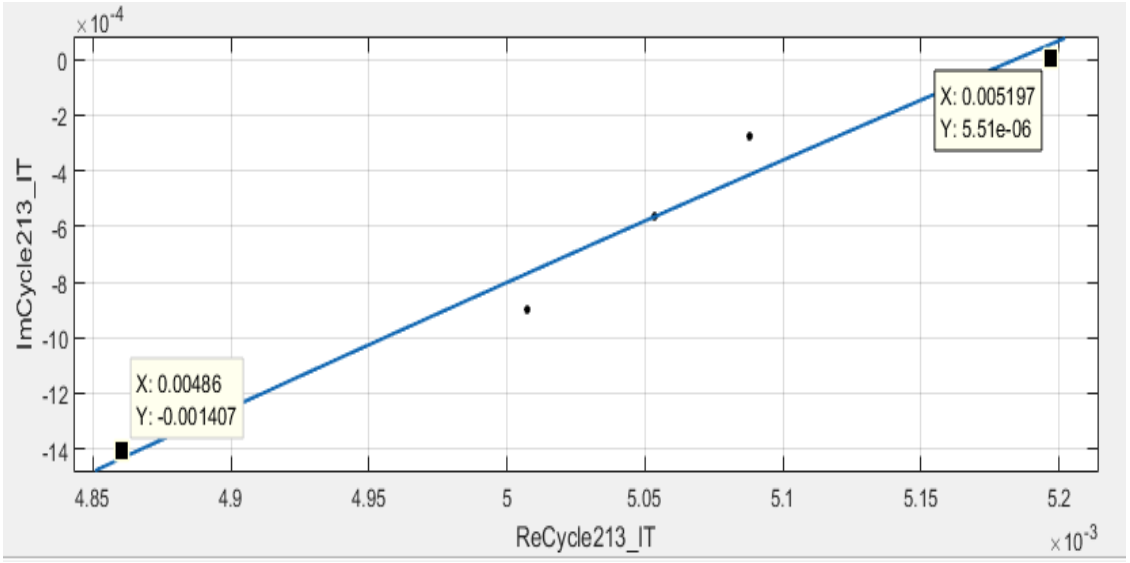

Figure 15: Inductive Tail of Cycle 213 Impedance with Reference Points

$$|Z| = \sqrt{(R_{arbitrary})^2 + \left(\frac{\omega}{Q_2}\right)^2} \rightarrow Q_2 = \omega * \left(\sqrt{(|Z|)^2 - (R_{arbitrary})^2}\right)^{-1}$$

$$|Z| = \sqrt{(X_{finalLength} - X_{InitialLength})^2 + (Y_{finalLength})^2}$$

$$|Z| = \sqrt{(0.00517 - 0.00486031)^2 + (0.00140696)^2} = 0.00144064$$

$$Q_2 = (2*\pi*1kHz) * \left(\sqrt{(0.00144064)^2 - (0.00517 - 0.00486031)^2}\right)^{-1}$$

$$Q_2 = 4.47MH^{-1}$$

$$L_2 = 0.22\mu H$$

$$n_2 = \sin(|\theta|) = \sin\left[\tan^{-1}\left(\frac{Y_{finalLength}}{X_{finalLength} - X_{InitialLength}}\right)\right] = 0.98$$

APPENDIX D

OPTIMIZED AND THEORETICAL ELEMENT VALUES

Cycle	1	213	309	345	419	465	863	881
C_{coat} (F)	2.22	7.07	6.98	3.49	5.25	8.11	12.56	5.26
R_{Ohm} (mΩ)	4.17	5.17	5.92	6.57	6.88	6.99	7.59	9.19
R_{CT} (mΩ)	1.16	0.54	0.37	0.49	0.73	0.47	0.20	0.49
Q_1 (F)	1066.42	267.51	287.86	138.18	278.99	303.87	2063.25	355.04
Q_2 (MH^{-1})	4.45	4.47	6.14	6.43	4.25	7.33	4.65	7.92
L (μH)	0.33	0.59	0.55	0.23	0.56	0.52	0.08	0.04
n_2	0.94	0.98	0.98	0.99	0.96	0.95	0.99	0.97
n_1	0.79	0.98	0.97	0.98	0.97	0.99	0.92	0.97

Table 7: Theoretical Electrical Component Values Created from Calculations

Cycle	1	213	309	345	419	465	863	881
C_{coat} (F)	6	7	12	7	7.5	15	33	7
R_{Ohmic} (mΩ)	4.22	5.19	5.93	6.59	6.91	7.05	7.56	9.19
R_{CT} (mΩ)	0.85	0.35	0.16	0.29	0.52	0.24	0.05	0.30
Q_1 (F)	900	272	280	136	282	300	2050	360
Q_2 (MH^{-1})	31.90	15.40	20	18	22.10	51	10.70	30
L (μH)	3	1	0.5	1.8	2	1	0.6	0.7
n_2	1.24	1.15	1.14	1.12	1.19	1.23	1.09	1.16
n_1	0.47	0.85	0.84	0.85	0.82	0.88	0.71	0.82

Table 8: Optimized Electrical Component Values

APPENDIX E

MAJOR AND MINOR OUTLIER ANALYSIS

	C_{coat} (F)	R_{Ohmic} (mΩ)	R_{CT} (mΩ)	Q_1 (F)	Q_2 (MH^{-1})	L (μH)	n_1	n_2
Median	7.25	6.75	0.29	900	21.10	1	0.83	1.15
1st Quartile	7	5.74	0.22	272	17.40	0.68	0.79	1.14
3rd Quartile	12.75	7.18	0.39	280	30.50	1.25	0.85	1.21
IQR	5.75	1.44	0.18	217	13.10	0.58	0.06	0.07
Lower Minor Error	-1.63	3.59	-0.05	-47.5	-2.33	-0.19	0.69	1.03
Upper Minor Error	21.38	9.33	0.66	820.50	50.20	2.11	0.94	1.31
Lower Major Error	-10.25	1.44	-0.31	-373	-22	-1.05	0.60	0.93
Upper Major Error	30	11.48	0.92	1146	69.90	2.98	1.04	1.41
Outlier indicator	No	No	Yes	Yes	Yes	Yes	Yes	No
Percent Error from Outliers	n/a	n/a	22.45 %	24.89 %	18.64%	11.77%	7.99%	n/a

Table 9: Minor and Major Outlier Analysis of Electrical Elements

APPENDIX F

CYCLE IMPEDANCE VERSE MODIFIED EEM DATA

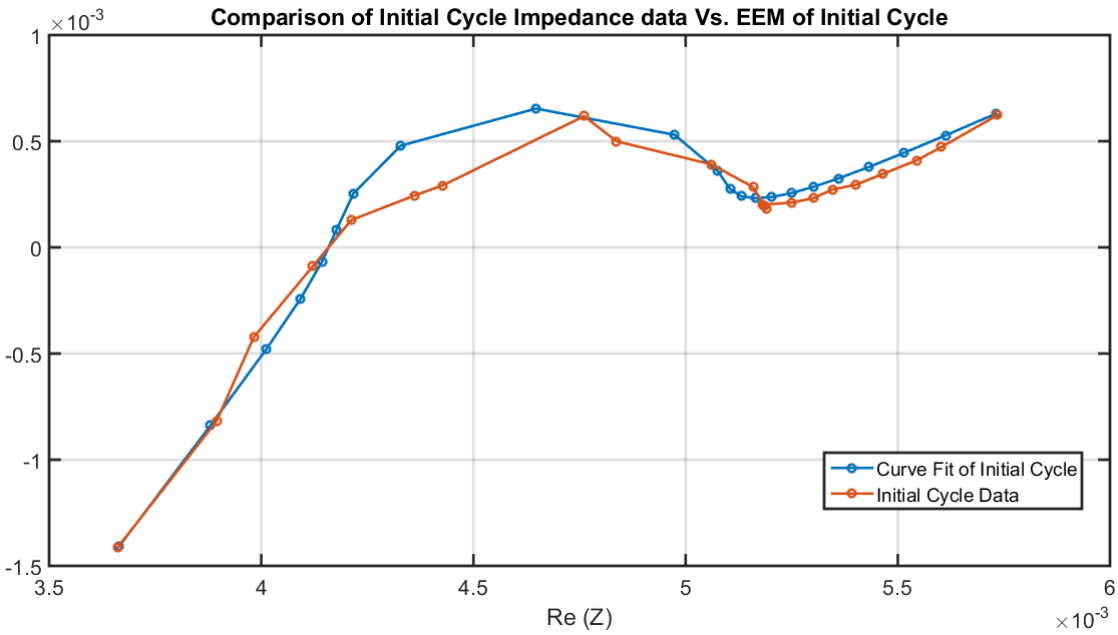

Figure 16: Initial Impedance Data Compared to the Results of the EEM

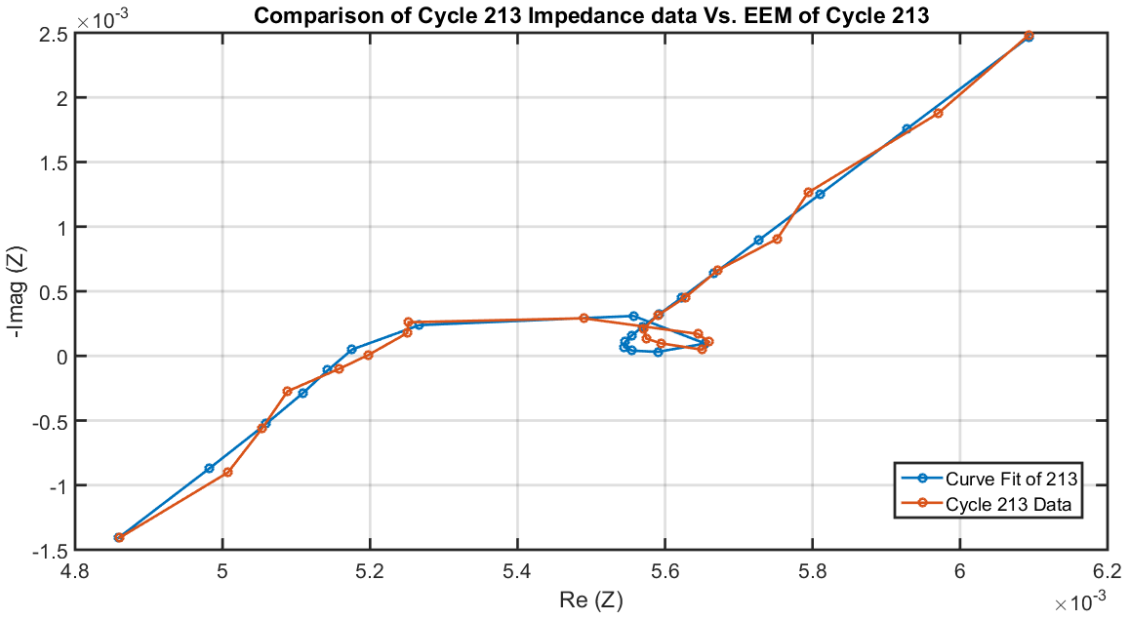

Figure 17: Cycle 213 Impedance Data Compared to the Results of the EEM

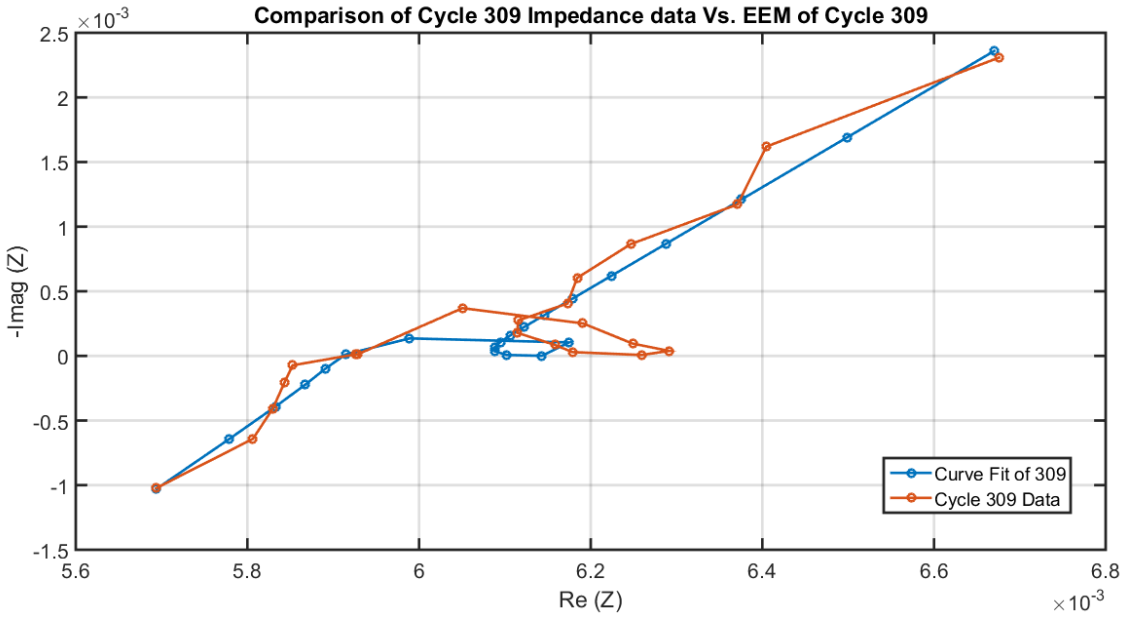

Figure 18: Cycle 309 Impedance Data Compared to the Results of the EEM

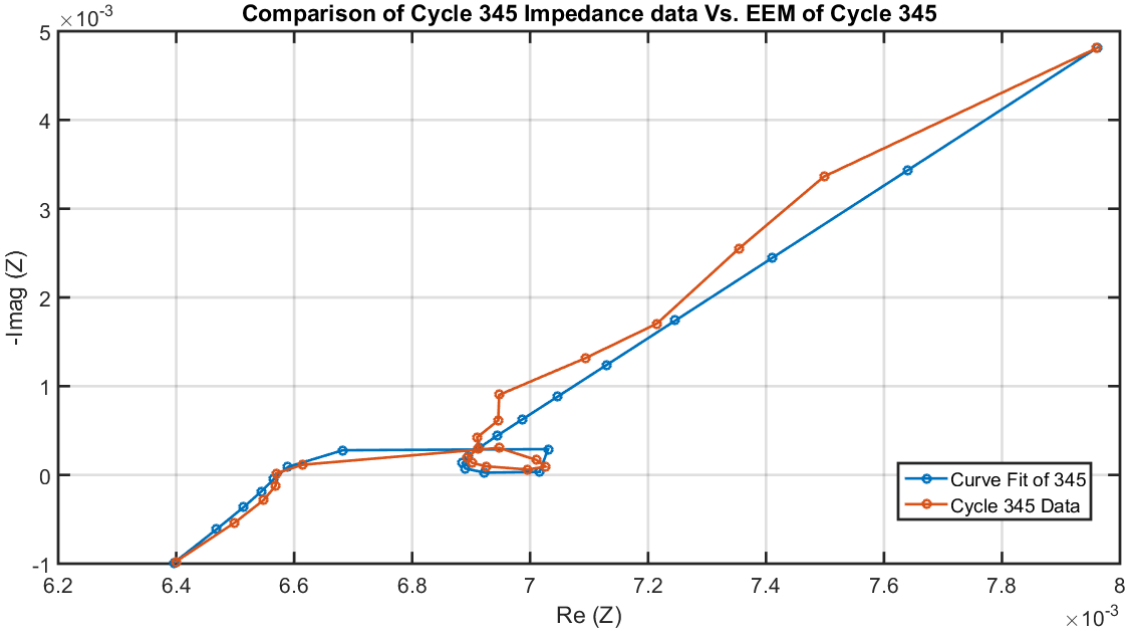

Figure 19: Cycle 345 Impedance Data Compared to the Results of the EEM

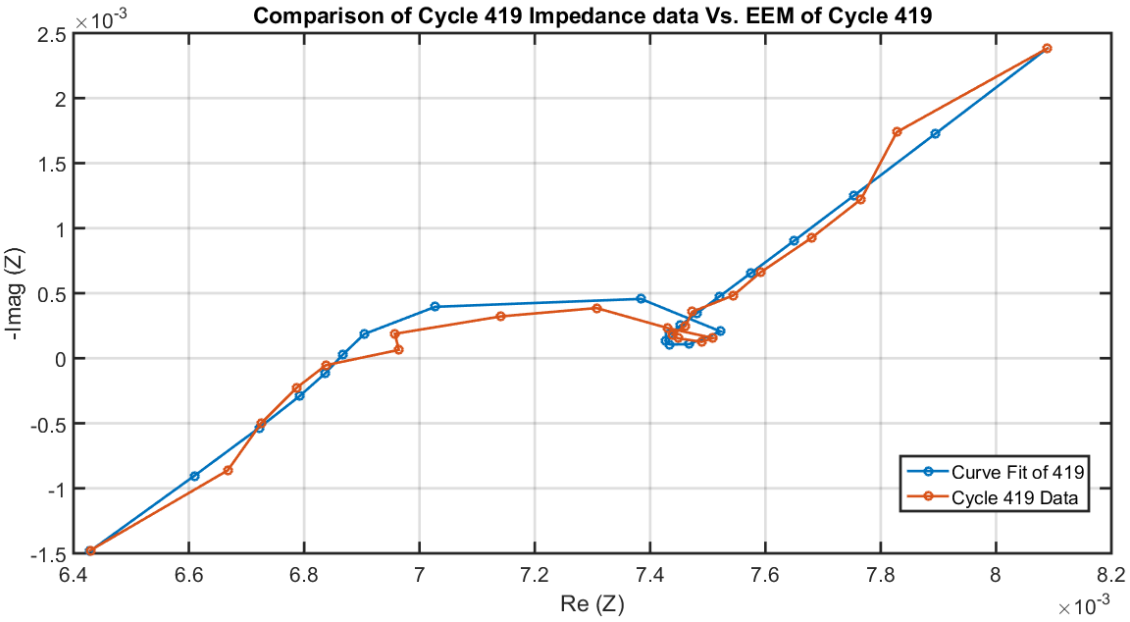

Figure 20: Cycle 419 Impedance Data Compared to the Results of the EEM

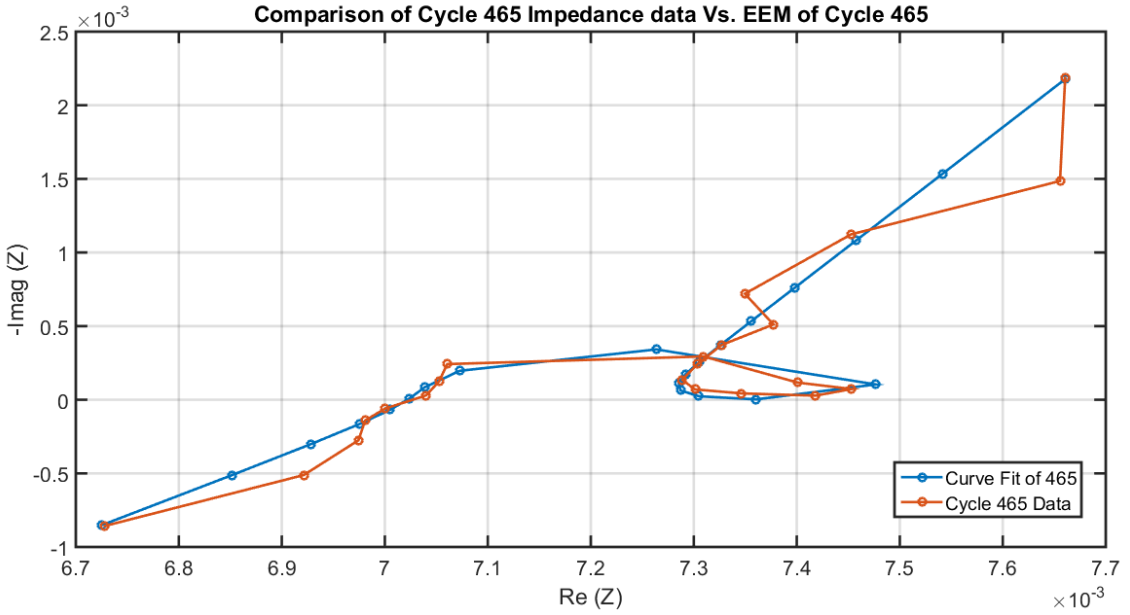

Figure 21: Cycle 465 Impedance Data Compared to the Results of the EEM

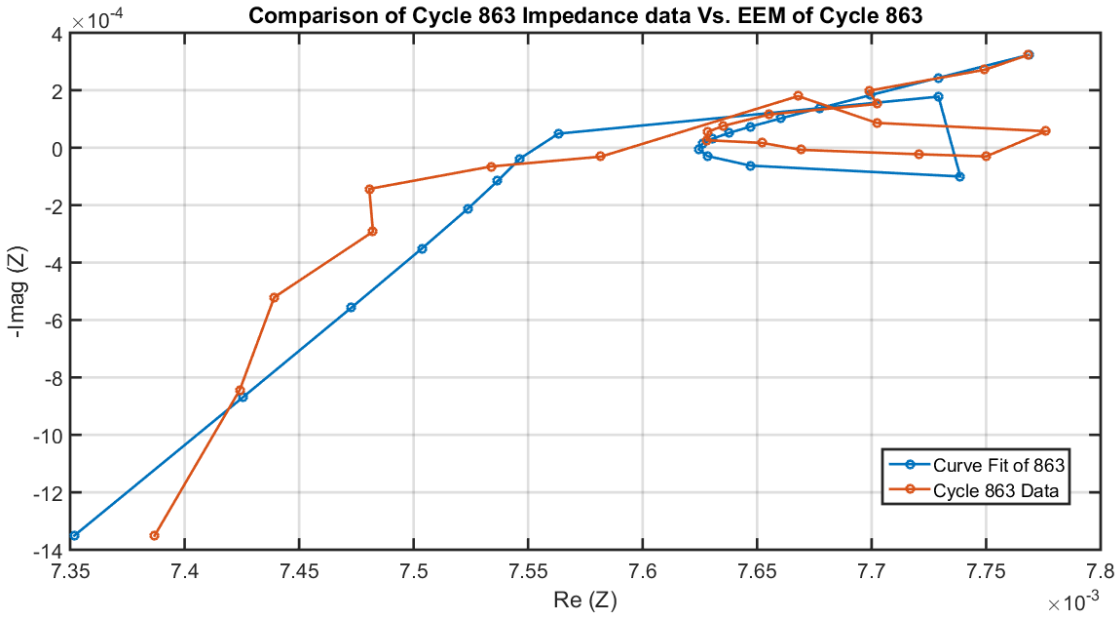

Figure 22: Cycle 863 Impedance Data Compared to the Results of the EEM

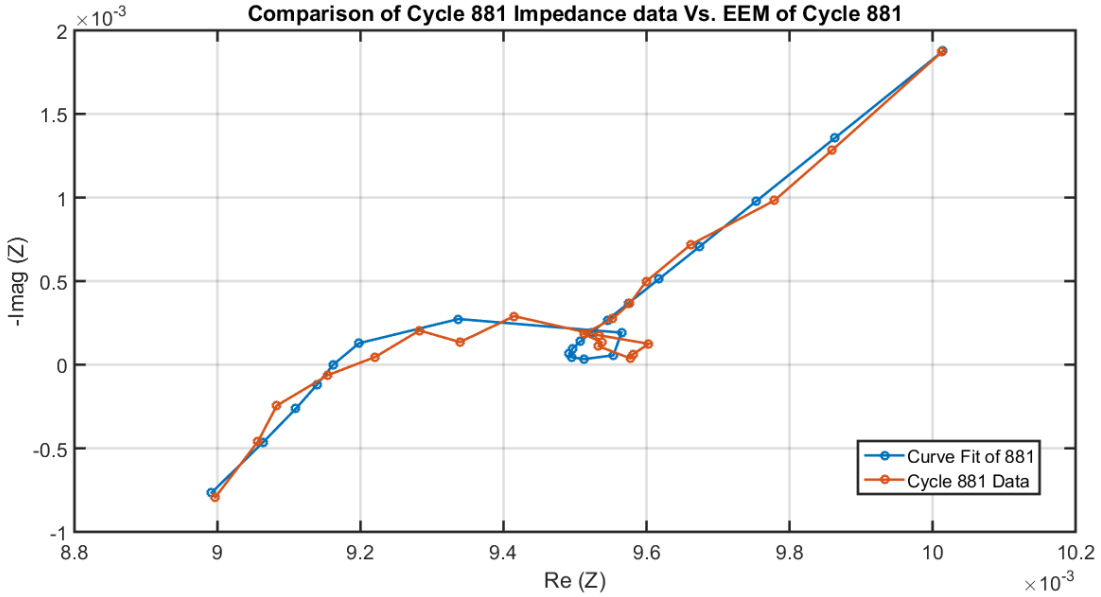

Figure 23: Cycle 881 Impedance Data Compared to the Results of the EEM

APPENDIX G

SAMPLE MATLAB CODE FOR DATA COMPARISON

```
% Variables for TF
C0 = 7;
R1 = 0.005194;
R2 = 0.00035;
Q1 = 1.54e7;
Q2 = 272;
L2 = 1e-6;
n1 = 1.1465;
n2 = 0.852;

Q = 2*pi*frequency(8:29); % defining omega from the raw data frequency

% Variables for R^2 values
x_data = ReHT_213_T1(8:29); % Extract x-axis impedance
y_data = ImHT_213_T1(8:29); % Extracting y-axis impedance
mean_x = mean(x_data);
mean_y = mean(y_data);
n = length(Q); % # of samples
p = 1; % # of predictors
% initializing values
SSE_X = 0;
SSE_Y = 0;
TSS_X = 0;
TSS_Y = 0;

% Variables used to break up transfer function calculations
A = zeros(length(Q),1);
B = zeros(length(Q),1);
C = zeros(length(Q),1);
D = zeros(length(Q),1);
E = zeros(length(Q),1);
F = zeros(length(Q),1);
G = zeros(length(Q),1);
H = zeros(length(Q),1);
I = zeros(length(Q),1);
J = zeros(length(Q),1);
K = zeros(length(Q),1);
L = zeros(length(Q),1);
M = zeros(length(Q),1);
N = zeros(length(Q),1);

% Variables used to seperate the real impedance from the imaginary
x = zeros(length(Q),1);
y = zeros(length(Q),1);

% Creating the impedance data from transfer function and omega above
```

```
for i = 1:length(Q)

        A(i) = ((j*Q(i))^(n2+1))*((R1*Q1*C0*R2*Q2)+(Q1*L2*Q2)); % s^(n2+1)
        B(i) = ((j*Q(i))^(n2+2))*(R1*Q1*C0*L2*Q2); % s^(n2+2)
        C(i) = ((j*Q(i)))*(R1*Q1*C0); % s
        D(i) = ((j*Q(i))^(n2))*((R1*Q1*Q2)+(Q1*R2*Q2)); % s^(n2)
        E(i) = ((j*Q(i))^(n2+n1+1))*(C0*R2*Q2); % s^(n1+n2+1;)
        F(i) = ((j*Q(i))^(n2+n1+2))*(C0*L2*Q2); % s^(n1+n2+2)
        G(i) = ((j*Q(i))^(n1+1))*(C0); % s^(n1+1)
        H(i) = ((j*Q(i))^(n1+n2))*(Q2); % s^(n1+n2)

        I(i) = ((j*Q(i))^(n2+1))*(Q1*C0*R2*Q2); % s^(n2+1)
        J(i) = ((j*Q(i))^(n2+2))*(Q1*C0*L2*Q2); % s^(n2+2)
        K(i) = ((j*Q(i)))*(C0*Q1); % s
        L(i) = ((j*Q(i))^(n2))*(Q2*Q1); % s^n2

        M(i) = A(i)+B(i)+C(i)+D(i)+E(i)+F(i)+G(i)+H(i)+Q1; % numerator
        N(i) = M(i)/(I(i)+J(i)+K(i)+L(i)); % Tranfser Function

end;
% seperating real/imag data
x = real(N);
y = -imag(N);

figure(1)
plot(x,y,'-o',x_data,y_data,'-o','LineWidth',2)
set(gca,'FontSize',16,'LineWidth',2)
legend('Curve Fit of 213','Cycle 213 Data');
xlabel('Re (Z)')
ylabel('-Imag (Z)')
title('Comparison of Cycle 213 Impedance data Vs. EEM of Cycle 213')
grid on

% Solving for variables needed in R^2 calculation with iteration
for w = 1:length(Q)

   SSE_X =((x_data(w)-x(w))^2)+SSE_X;
   SSE_Y = ((y_data(w)-y(w))^2)+SSE_Y;
   TSS_X = ((x_data(w)-mean_x)^2)+TSS_X;
   TSS_Y = ((y_data(w)-mean_y)^2)+TSS_Y;

end

% R^2 values
R_Squared_X = 1-(SSE_X/TSS_X);
R_Squared_Y = 1-(SSE_Y/TSS_Y);
```